J. Mech. Phys. Solids 186 (2024) 105602

Contents lists available at ScienceDirect

Journal of the Mechanics and Physics of Solids

journal homepage: www.elsevier.com/locate/jmps

# Configurational force method enables fracture assessment in soft materials

Miguel Angel Moreno-Mateos [a,*], Paul Steinmann [a,b]

[a] Institute of Applied Mechanics, Friedrich-Alexander-Universität Erlangen–Nürnberg, Egerlandstr. 5, 91058, Erlangen, Germany
[b] Glasgow Computational Engineering Centre, School of Engineering, University of Glasgow, G12 8QQ, United Kingdom

ARTICLE INFO

*Keywords:*
Configurational mechanics
Material forces
Soft fracture
Finite strains
Numerical methods
Experimental mechanics

ABSTRACT

Configurational mechanics offers a framework for quantifying the tendency of defects to alter the material configuration. When applied to fracture mechanics, configurational forces can be used to quantify the propensity of cracks to propagate. An alternative, well-established approach involves analytical solutions for crack tip displacement fields. However, these solutions typically apply to a limited range of constitutive behaviors and oftentimes to the linear small strain regime. The ease of calculating configurational forces in a numerical Finite Element implementation, along with their applicability to soft fracture at large strains, motivates the study of their performance as a standalone fracture framework. In contrast to the majority of works that remain theoretical and numerical, our study includes a robust experimental approach to configurational forces at finite strains. We report tensile experiments on a soft elastomer with pre-cuts ante fracture initiation. In a first attempt to approach the $J$-integral via configurational forces, we explore the performance of the linear elastic fracture mechanics solutions on Pacman-shaped domains that reproduce the crack tip vicinity. Then, we implement the entire boundary value problem with three-dimensional simulations that replicate the empirical tensile deformation of the soft elastomer samples. Subsequently, the results are benchmarked against estimations of the $J$-integral obtained through a bespoke finite strain analytical crack tip solution. With the successful validation of the configurational force method at finite strains, we aim to establish a pipeline for the calculation of configurational forces in a standalone manner and circumventing the need for close-form analytical solutions.

## 1. Introduction

"*What can the configurational force method tell about the $J$-integral?*" This question has been fundamental in prior works in the scope of configurational mechanics. Now, it can be extended: "*Can the configurational force method be applied to soft materials to calculate $J$ at large deformations?*" and most important, "*are the results trustworthy?*"

Configurational mechanics provides a framework to quantify the tendency of defects to modify the material configuration (Eshelby, 1951; Steinmann, 2000; Gross et al., 2003; Steinmann et al., 2009; Steinmann, 2022). These changes in material positions align with a postulate of maximum energy dissipation. The energy released during these modifications can be expressed in terms of configurational forces, which are either power-conjugated or variationally conjugated to changes in the material configuration. Consequently, configurational forces are driving forces that act on the material manifold, leading to modifications in the material positions. These forces are necessary to understand the reaction of a body to the evolution of defects (Podio-Guidugli, 2002).

* Corresponding author.
*E-mail address:* miguel.moreno@fau.de (M.A. Moreno-Mateos).

https://doi.org/10.1016/j.jmps.2024.105602
Received 13 November 2023; Received in revised form 31 January 2024; Accepted 10 March 2024
Available online 12 March 2024

Advanced applications of soft materials require robust solutions to withstand damage. Soft materials[1] exhibit various failure mechanisms, including cavitation (Lefèvre et al., 2015; Fu et al., 2020; Chen and Yang, 2022), fatigue (Tang et al., 2017; Bai et al., 2019; Li et al., 2020; Sanoja et al., 2021; Zheng et al., 2022), and fracture (Pharr et al., 2012; Taylor et al., 2012; Long and Hui, 2016; Chen et al., 2017; Hesch et al., 2017; Russ et al., 2020; Yin et al., 2021; Xue et al., 2023), among others. Significant deformations in applications like fatigue-resistant ligaments (Li et al., 2022), soft polymer-based skin patches (Theocharidis et al., 2022), wound closure meshes (Gao et al., 2021), bioadhesive skin sensors (Wang et al., 2022; Ma et al., 2022), and skin-inspired hydrogels (Yuk et al., 2016), can initiate and propagate cracks (Creton and Ciccotti, 2016). Chen et al. (2017) discussed the effect of pre-cuts on a soft elastomer and its stretching behavior until rupture. More recently, Moreno-Mateos and co-authors proposed magneto-active elastomers with enhanced fracture performance through magneto-mechanical coupling (Moreno-Mateos et al., 2023b) and soft dielectric elastomers with modulation of the fracture performance via electro-mechanical actuation (Moreno-Mateos et al., 2024). Within this context, investigating flaw sensitivity of highly stretchable materials remains an active area of research. Only with a thorough understanding of the intricacies of soft fracture can failure-tolerant applications be developed.

Established theories to assess fracture mechanics include the energy release rate (Griffith, 1921), the stress intensity factors (Irwin, 1957), the $J$-integral (Cherepanov, 1967; Rice, 1968; Shih et al., 1986), and crack tip opening displacement (Wells, 1961). As crack deflection criteria for scenarios involving mixed-mode crack propagation, the maximum tangential stress strategy (Erdogan and Sih, 1963), the strain–energy-density S-factor (Sih, 1974), the maximum energy release rate (Hussain et al., 1974), and the apparent crack extension force criterion (Strifors, 1974) have been proposed. All these well-known strategies have been mostly deployed in the domain of Linear Elastic Fracture Mechanics (LEFM), restricted to materials characterized by linear elasticity and moderate strains. However, when it comes to soft elastomers, their behavior introduces unique challenges. At finite deformations, the crack tip undergoes significant blunting (Hui et al., 2003; Qi et al., 2019; Lu et al., 2021). In this regard, only a few close-form solutions address soft fracture with analytical descriptions of the crack contour and crack tip vicinity after deformation (Long et al., 2011; Long and Hui, 2015).

Computational fracture mechanics encompasses various strategies, some of them grounded in the Griffith-type energy functional and variational formulation introduced by Francfort and Marigo (1998). Non-local damage models use a history variable and a non-local equivalent strain (Schreyer, 1990; Peerlings et al., 1998; Jirásek, 1998). A strain measure governs the evolution of damage. The element deletion method is one of the simplest approaches for fracture simulation within the framework of the conventional FEM (Song et al., 2008). The FE mesh needs to be modified during propagation and crack propagation is considerably mesh dependent. With its origin on the cohesive forces which occur when material elements are being pulled apart (Dugdale, 1960), cohesive zone models enable crack propagation through the separation of the surfaces in an extended crack tip zone (Park and Paulino, 2011; Marigo, 2023; Baktheer et al., 2024). The direction for crack propagation is also restricted by the FEM mesh and branching is not allowed. The extended finite element method enriches the solution functional space to admit discontinuous functions (Moës et al., 1999). This modeling approach reduces mesh dependency and eliminates the need to update the FE mesh to track the crack path. The element-free Galerkin method is a mesh-free model based on moving least-square interpolants where only nodal data, and not element connectivity, is needed (Belytschko et al., 1995). No remeshing is required to treat a moving crack but the method does not easily reproduce branching. Phase-field methods for fracture allow for a continuum treatment of the region through a damage field and a non-local field equation. Among many others, Heider (2021), Kalina et al. (2023), Li et al. (2023) can be consulted. The approach to model the crack as a regularized diffusive crack enables a continuous treatment of the fracture and a reduced mesh dependence. The crack direction is unrestricted and remeshing strategies can be employed to reduce the computational cost, yet guaranteeing the physical consistency of the method. Some existing works advocate energy splits to prevent unphysical crack nucleation and propagation at compression loads (Miehe et al., 2010b,a). Some others incorporate the notion of crack nucleation with additional external driving forces (Kumar et al., 2020a; Larsen et al., 2024). Recently, the phase-field method has been applied to large structures (Lo et al., 2022). Eigenfracture is based on the spectral decomposition of the strain energy through the definition of an eigenstrain tensor that captures deformations in the presence of a crack (Schmidt et al., 2009; Fan et al., 2021; Storm and Kaliske, 2023a). This method has been used, e.g., in conjunction with the material point method (Chihadeh et al., 2023) and permits to model fracture in large deformation problems. Peridynamics frameworks for fracture are based on a discrete non-local adaptation of classical continuum mechanics (Silling, 2000; Diehl et al., 2022; Javili et al., 2021). The formulation via interaction forces between material points facilitates capturing singularities. The method allows for complex fracture patterns, albeit originally with limitations in the Poisson's ratio. An alternative discrete modeling approach concerns lattice models, e.g., the one by Braun et al. (2024) based on linear and angular springs. The aforementioned methods are just a few examples among many others. Overall, as described by Storm and Kaliske (2023b), energetically motivated fracture methods are frequently argued based on advantages regarding meshing, crack nucleation, propagation, and branching, cohesive and fatigue failure, as well as the possibility to model processes at the crack gap like friction and heat radiation.

The capabilities of configurational mechanics to describe various types of material inhomogeneities within the continuum mechanics framework explain its widespread application in numerous fields. Notable examples include the description of dislocations and crystal plasticity (Peach and Koehler, 1950; Steinmann, 2002; Menzel et al., 2004, 2005; Baxevanakis and Giannakopoulos, 2015), remeshing or r-adaptivity methods (Braun, 1997; Hénap and Szabó, 2017), homogenization (Ricker et al., 2010), nonlinear structural dynamics (Armanini et al., 2019), and its role in understanding forces driving biomechanics growth (Kuhl et al., 2004;

[1] We use the term "soft material" to refer to compliant materials with a stiffness below 100 kPa, such as in the case of the elastomeric matrix for ultra-soft magneto-rheological elastomers in Moreno-Mateos et al. (2022, 2023a).

Kuhl and Steinmann, 2004; Kirchner and Lazar, 2007; Goda et al., 2016). Nevertheless, it is in the field of fracture mechanics where configurational mechanics finds the most extensive applications. The domain integral representation of the celebrated $J$-integral, which is based on the virtual crack extension technique (Shih et al., 1986), is mathematically identical to the configurational force approach. Inter alia, Steinmann et al. (2001), Kienzler et al. (2002), Denzer et al. (2003), and Gurtin and Podio-Guidugli (1996) have postulated laws for crack propagation based on configurational mechanics, where configurational mechanics can provide a fracture criterion (Zhou et al., 2022). Schütte (2009) and Frankl et al. (2022) have explained curved crack propagation using configurational forces and Kolednik et al. (2010) the effects of interfaces on crack propagation and configurational forces. Moreover, Steinmann (2008) described the role of dissipative configurational tractions on boundaries and the duality of forces within deformational and configurational mechanics, at surfaces, curves, and points. Based on the momentum balance of the Eshelby stress tensor, Fischer et al. (2012) described configurational forces at boundaries in fracture mechanics problems and related these force distributions to the $J$-integral. Further applications include Ozenc et al.'s exploration of crack branching in dynamic brittle fracture (Özenç et al., 2016) and Guo and co-authors' proposal of a configurational forces-based criterion for mixed-mode crack propagation (Guo and Li, 2017). Configurational mechanics has also been extended to address fatigue failure (Liu et al., 2020), with some works integrating the framework with phase field models (Yan et al., 2023). Additionally, inelastic behavior in fracture mechanics has been addressed, including inelastic material behavior (Nguyen et al., 2005; Näser et al., 2007; Kaliske et al., 2009) and elasto-plastic creeping materials (Özenç et al., 2014; Kolednik et al., 2022). To a further extent, configurational mechanics has also found applications in coupled problems. In this respect, Denzer and Menzel (2014) explored electro-viscoelastic fracture mechanics and Kuhl et al. (2004) established a framework for thermo-hyperelastic fracture. Lastly, configurational peridynamics is a recent approach to fracture mechanics, based on the description of Piola-type and Cauchy-type bond-wise interaction forces (Steinmann et al., 2023). The method leverages configurational forces as a fracture criterion in a peridynamic framework for fracture. These examples represent a selection of the numerous works that approach fracture mechanics from a configurational vista.

The advancement in configurational mechanics raises the question of whether configurational forces can serve as a standalone and sufficient framework to describe fracture mechanics of soft materials at finite strains. To be successful, the calculation of configurational forces at the crack tip must yield a value equal to the $J$-integral. Subsequently, and for pure mode-I loading, the configurational force method will allow to circumvent the calculation of the line integration of the Eshelby traction to determine the $J$-integral. In the more general case of mode-I/II loading in plane problems or mode-I/II/III in a 3D problem, the determination of the configurational forces requires the calculation of line integrals along the crack faces (Schmitz and Ricoeur, 2023). Furthermore, using configurational forces at finite strains, rather than relying on analytical crack tip solutions, holds promise for accurately capturing the behavior at large deformations. Here, the results may be as accurate as the constitutive model utilized to solve the boundary value problem (BVP). Within this context, only a few works have explored the behavior of configurational forces in a three-dimensional setting (Schmitz and Ricoeur, 2023), and only some have combined experiments and numerics (Guo and Li, 2017). Moreover, to the best of the authors' knowledge, no work has benchmarked the performance of configurational forces against experiments on soft materials. We believe that this is a crucial undertaking to enable the use of the configurational force method in soft fracture applications and to eliminate the reliance on analytical solutions.

In this study, our primary aim is to address the existing challenges associated with the use of configurational forces in the context of finite strains. To achieve this goal, we present an integrated approach that combines numerical simulations and experimental investigations conducted on a soft elastomer material. In the experimental setting, precut samples made of a soft elastomer are tested under tensile deformation. This is on the basis for the calibration of the constitutive model and for the digital image correlation (DIC) analysis to explore the deformation of the crack tip vicinity. Subsequently, the configurational forces are calculated from BVPs designed to replicate the experimental samples featuring initial pre-cuts. To ensure that the deformation at the crack tip vicinity replicates the experimental observations, we calculate the error between the numerical and experimental displacement fields. Eventually, the configurational forces are validated with numerically-estimated values of the $J$-integral. These estimations of $J$ are based on displacement fields solved in the boundary value problem and the finite strain solutions of Long and Hui (2015), during the loading event and ante crack onset.[2] Our primary objective is to validate the configurational force method and demonstrate its effectiveness as a substitute for the conventional approaches to calculate the $J$-integral at finite strains. By achieving this validation, we aim to pave the way for future applications where configurational forces can be calculated using advanced constitutive modeling, serving as a standalone framework for finite strain analyses.

This manuscript is organized as follows. To set the stage, the experimental setting and the soft elastomer investigated are presented in Section 2. Then, the continuum mechanics framework is given in Section 3. The constitutive framework to solve the direct motion problem is addressed first, followed by a brief recap of configurational mechanics. These provide the background for the Finite Element (FE) BVP and the foundations for the calculation of the configurational forces. Then, Section 4 presents a preliminary, yet highly instructive, approach to the relationship between the configurational forces and $J$ within the scope of LEFM. The most interesting finding here is the relatively high accuracy of a linear elastic crack model even in the case of large deformations, where the prerequisites for asymptotic crack tip fields of LEFM are intuitively expected to be severely violated. We employ three-dimensional Pacman-shaped domains to replicate the crack tip vicinity. Afterwards, the real samples and the tensile loading test motivate the calculation of configurational forces in Section 5 using a BVP that replicates the real experiment. Section 6 offers a validation of the configurational force method with values of $J$ estimated from the numerical displacement fields of the BVP and finite strain crack tip solutions. Lastly, in Section 7, we provide a comprehensive discussion and an outlook for future research.

[2] Note that it is not the object of this work to explore the evolution of the material configuration during crack propagation, but only up to crack onset.

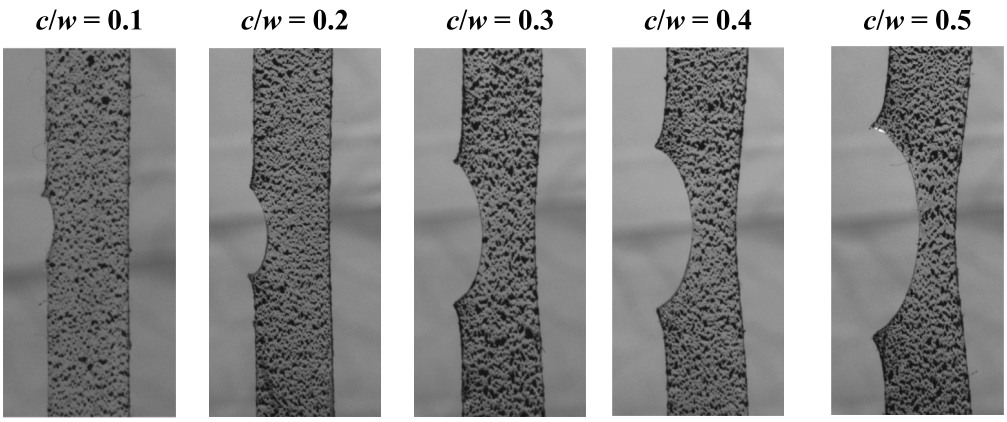


**Fig. 1. Deformed VHB samples featuring pre-cuts and with a surface speckle pattern ante fracture onset.** The low stiffness and high stretchability of the elastomer produces a blunt crack contour. The application of a speckle pattern is fundamental for the digital image correlation (DIC) analysis.

## 2. Experimental observations

The experimental determination of the $J$-integral has been pursued in numerous prior works, including the studies by Hocine et al. (2002), Ma et al. (2006), Simha et al. (2008), Barati et al. (2010), and Hedan et al. (2011), among others. Customary experimental approaches based on DIC to estimate $J$ require the differentiation of the displacement fields to obtain the strain fields, apply constitutive arguments to estimate the stress fields, and eventually perform the contour integral of the Eshelby stress (Vavrik and Jandejsek, 2014). This conventional approach entails several drawbacks, namely that the use of two-dimensional DIC displacement fields to calculate a stress field can lead to important deviations from the real structural behavior. In this work, we propose a more convenient alternative method based on the configurational force method (Steinmann et al., 2001). To embark on this approach, we begin by introducing the experimental setting, which lays the groundwork for understanding the challenges and establishing the foundation for calculating $J$. The experimental framework involves the use of soft elastomeric samples with pre-cuts, tensile tests, and DIC analysis.

A set of tensile tests were performed on the soft elastomer VHB$^{TM}$ 4905 tape (3M$^{TM}$, Saint Paul, Minnesota, United States) (Ahmad et al., 2019; Liao et al., 2020). Rectangular samples were prepared with a width ($w$) of 10 mm, and thickness ($t$) of 0.5 mm. With the use of a blade, pre-cuts of different lengths were applied on the samples. The crack-width ratio ($c/w$) parameter, defined as the length of the pre-cut divided by the width of the sample, takes the values of $0.1$, $0.2$, $0.3$, $0.4$, and $0.5$ to refer to the pre-cuts of lengths ($c$) of 1 mm, 2 mm, 3 mm, 4 mm, and 5 mm, respectively. Next, the surface of the sample is coated with a speckle pattern to allow for DIC analysis. The pattern is applied with acrylic black spray paint and renders a resolution of 0.2 mm. Fig. 1 showcases the surface speckle pattern on deformed samples.

Once the samples are prepared, they are mounted in an universal tensile machine (Inspekt S 5 kN, Hegewald & Peschke, Nossen, Germany) with an initial distance between the clamps of $l_0 = 30\,\text{mm}$ and are tested with a quasi-static constant loading rate of $\dot{y} = 0.02\,\text{mm}\,\text{s}^{-1}$ or, in an alternatively terminology, a strain rate ($\dot{y}/l_0$) of $6.7 \times 10^{-4}\,\text{s}^{-1}$. The force–displacement data are stored during the test and up to full rupture. Fig. 2 shows the results as tensile curves for all the crack-width ratios after five repetitions for each test condition.

During the tensile tests, images of the surface of the samples are acquired. A monochromatic CCD sensor (DCS 2.0, LIMESS Messtechnik & Software GmbH, Germany) with a resolution of $1024 \times 768$ and a lens with focal range $\geqslant 50\,\text{mm}$ and aperture 2.8-16 (2.8/50-0902 Xenoplan, Schneider Kreuznach, Bad Kreuznach, Germany) were used to capture the crack tip and surrounding area during the deformation of the sample. Afterwards, the open source Matlab NCorr suite (Blaber et al., 2015) was used to calculate the displacement fields, with a resolution of 0.07 mm/pixel. The analysis is performed with a subset radius of 12 pixel, in a backward manner setting the initial region of interest on the final deformed picture in order to facilitate the identification of the crack contour, and updating the reference image (as well as the region of interest) to deal with the large strains.

The DIC fields are associated with specific loading stages (displacement of the clamp) ante crack onset and are grouped according to the crack-width ratio. Fig. 3 presents five illustrative examples for displacements of 112 mm, 78 mm, 61 mm, 59 mm, and 48 mm, respectively for $c/w$ values from 0.1 to 0.5. The Lagrangian displacement fields ($u_y$) in Fig. 3a are presented after an offset correction that renders null vertical displacement at the crack tip. In addition, the yy-component of the Euler–Almansi[3] strain field ($e_{yy}$) is calculated and shown in Fig. 3b by differentiating the displacement fields. It can be observed how the strain concentration at the crack tip vicinity increases with the length of the pre-cut.

In the next section, we will describe the continuum mechanics and numerical frameworks necessary for calculating configurational forces via the configurational force method.

[3] The Euler–Almansi strain field referenced to the spatial configuration is defined as $\mathbf{e} = \frac{1}{2}\left[\mathbf{i} - \mathbf{b}^{-1}\right]$, with $\mathbf{i}$ the second-order identity tensor and $\mathbf{b} = \mathbf{F} \cdot \mathbf{F}^{T}$ the left Cauchy–Green deformation tensor.

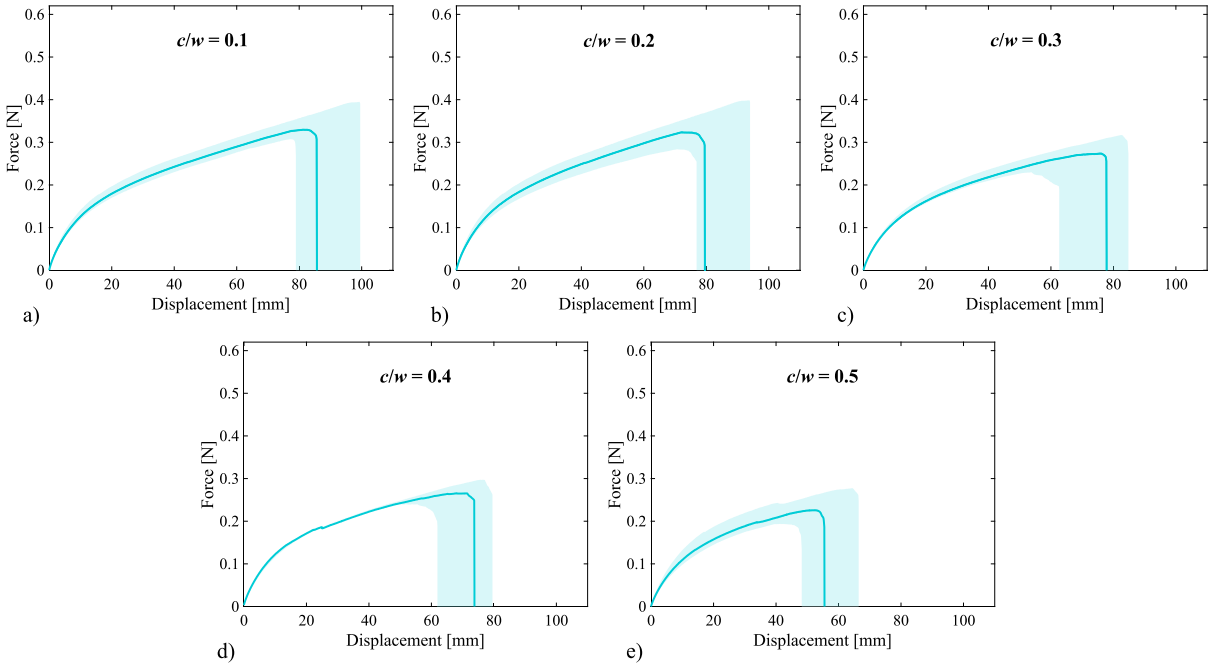


**Fig. 2. Results for tensile tests up to fully rupture of elastomeric samples.** (a) Force–displacement curves from tensile tests on samples feature pre-cuts with crack-width ratios $c/w = \{0.1, 0.2, 0.3, 0.4, 0.5\}$. The shaded areas quantify the scatter of the experimental results: five experiments are performed for each test condition.

## 3. Continuum mechanics: constitutive and numerical framework

The kinematic description of a continuum involves establishing a relationship between the positions of physical points before and after the application of load. In the absence of loads, the state of the continuum is defined by the material positions in the material configuration. After undergoing deformation due to external loads, the spatial positions of the continuum in the spatial configuration need to be determined. The parametrization of the kinematic and energetic quantities in terms of the material positions is commonly known as *spatial motion problem* or rather as *deformational mechanics*. In the *material motion problem* or rather *configurational mechanics*, the kinematic and constitutive measures are akin to those employed in the direct motion description but are parametrized in terms of the spatial positions of the continuum. Central to configurational mechanics is the notion of a stress–energy tensor, which is related to configurational forces. Just as spatial forces are associated with the deformation of the continuum, configurational forces drive changes in the material configuration, leading to an associated release of energy.

### 3.1. Spatial motion problem: Kinematics, balance laws, and constitutive relations

The deformation of the medium is formulated in a finite strain framework. In the spirit of the spatial or direct motion description, the displacement field $\mathbf{u}(\mathbf{X})$ maps the positions in the material configuration $\mathbf{X} \in \Omega_0$, with boundary $\partial\Omega_0$, to the positions in the spatial configuration $\mathbf{x} \in \Omega$ according to $\mathbf{x} = \boldsymbol{\varphi}(\mathbf{X}) = \mathbf{u}(\mathbf{X}) + \mathbf{X}$. The deformation gradient is defined as $\mathbf{F} = \nabla_0 \mathbf{u} + \mathbf{I}$, with $\mathbf{I}$ the second-order identity tensor and $\nabla_0$ the gradient operator in the material configuration. Fig. 4 illustrates the direct kinematic description. Following the multiplicative isochoric-volumetric decomposition $\mathbf{F} = \mathbf{F}_{\text{vol}} \cdot \overline{\mathbf{F}}$, the volumetric part is defined as $\mathbf{F}_{\text{vol}} = [\det \mathbf{F}]^{1/3}\, \mathbf{I}$ and the isochoric part as $\overline{\mathbf{F}} = [\det \mathbf{F}]^{-1/3}\, \mathbf{F}$, where $\det \mathbf{F}$ denotes the determinant of $\mathbf{F}$.

The energy density per undeformed volume of the system consists of isochoric and volumetric contributions, according to a decoupled representation

$$\Psi(\mathbf{F}) = \Psi_{\text{iso}}(\overline{\mathbf{F}}) + \Psi_{\text{vol}}(\det \mathbf{F}). \tag{1}$$

The potential energy functional $\Pi$ is defined as

$$\Pi(\mathbf{u}) = \Pi_{\text{int}}(\mathbf{u}) + \Pi_{\text{ext}}(\mathbf{u}) = \int_{\Omega_0} \Psi(\mathbf{F}(\mathbf{u}))\, \mathrm{d}V - \int_{\Omega_0} \mathbf{b}_0 \cdot \mathbf{u}\, \mathrm{d}V - \int_{\partial\Omega_0} \mathbf{t}_0 \cdot \mathbf{u}\, \mathrm{d}A, \tag{2}$$

with $\mathbf{b}_0$ and $\mathbf{t}_0$ the body and surface forces, respectively.

The governing field equation can be obtained through the principle of stationary potential energy, which requires that the first variation of the total potential energy functional vanishes for any admissible virtual displacement $\delta\mathbf{u}$,

$$\delta_{\mathbf{u}}\Pi = \left.\frac{\mathrm{d}}{\mathrm{d}\lambda}\Pi(\mathbf{u} + \lambda\delta\mathbf{u})\right|_{\lambda=0} = \int_{\Omega_0} \frac{\partial \Psi(\mathbf{F}(\mathbf{u}))}{\partial \mathbf{F}} : \nabla_0 \delta\mathbf{u}\, \mathrm{d}V - \int_{\Omega_0} \mathbf{b}_0 \cdot \delta\mathbf{u}\, \mathrm{d}V - \int_{\partial\Omega_0} \mathbf{t}_0 \cdot \delta\mathbf{u}\, \mathrm{d}A \overset{!}{=} 0. \tag{3}$$

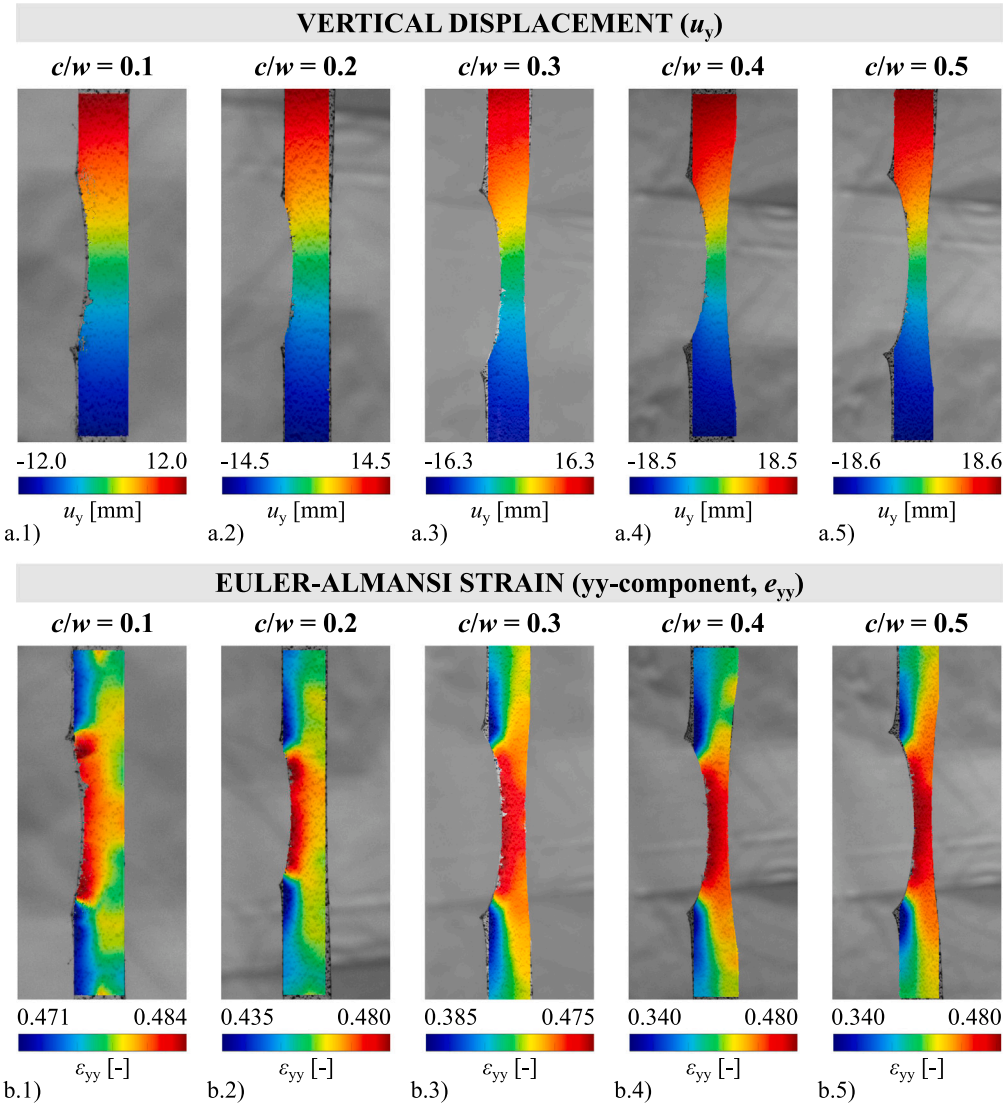


**Fig. 3. Displacement and strain fields obtained via digital image correlation on VHB samples featuring different pre-cuts.** The fields are depicted in the spatial (deformed) configuration, i.e., Euler displacement field and Euler–Almansi strain field, and correspond to a total displacement of each sample of 112 mm, 78 mm, 61 mm, 59 mm, 48 mm, respectively for the crack-width ratios ($c/w$) of 0.1, 0.2, 0.3, 0.4, and 0.5.

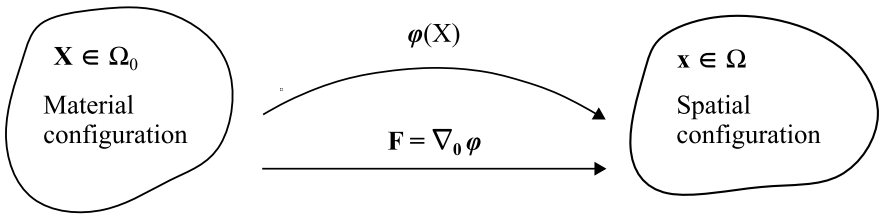


**Fig. 4. Kinematics of the spatial motion problem.** The direct deformation map and direct deformation gradient relate the material configuration ($\Omega_0$) to the spatial configuration ($\Omega$).

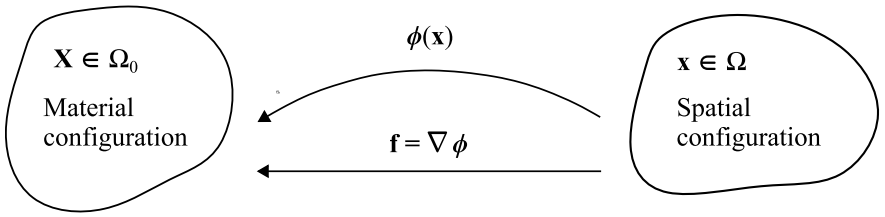


**Fig. 5. Kinematics of the material motion problem.** The reverse deformation map and reverse deformation gradient relate the spatial configuration ($\Omega$) to the material configuration ($\Omega_0$).

From the previous requirement, in the absence of body and surface forces, and identifying the Piola stress tensor as $\mathbf{P} = \partial_{\mathbf{F}} \Psi(\mathbf{F}(\mathbf{u}))$, the field equation reads

$$\boldsymbol{\nabla}_0 \cdot \mathbf{P} = \mathbf{0}, \tag{4}$$

with $\boldsymbol{\nabla}_0 \cdot$ the divergence operator in the material configuration.

Next, let us define the constitutive relations. The isochoric contribution in Eq. (1) is here defined by the Generalized neo-Hookean (GNH) model as a function of the isochoric deformation gradient,

$$\Psi_{\text{iso}}\left(\overline{\mathbf{F}}\right) = \frac{G}{2b}\left[\left[1 + \frac{b}{n}\left[\mathbf{I} : \left[\overline{\mathbf{F}}^{\mathrm{T}} \cdot \overline{\mathbf{F}}\right] - 3\right]\right]^{n} - 1\right], \tag{5}$$

where $G = 3$ kPa is the shear modulus and $n = 1.05$ and $b = 1.05$ are parameters of the GNH model calibrated in Appendix A for the acrylic polymer VHB$^{\text{TM}}$ 4905 tape.

Furthermore, the volumetric contribution is a function of the Jacobian of the deformation gradient,

$$\Psi_{\text{vol}}(\det \mathbf{F}) = \frac{\kappa}{2}\left[\det \mathbf{F} - 1\right]^2, \tag{6}$$

with bulk modulus $\kappa = 100\,\text{kPa}$, chosen several orders larger than $G$ on the argument that polymer materials are nearly incompressible. For VHB tape, Hossain et al. (2012) can be consulted.

The Piola stress tensor can be derived from the energy density as the addition of isochoric and volumetric contributions, $\mathbf{P} = \mathbf{P}_{\text{iso}} + \mathbf{P}_{\text{vol}}$, where the isochoric contribution is obtained as

$$\mathbf{P}_{\text{iso}} = \frac{\partial \Psi_{\text{iso}}\left(\overline{\mathbf{F}}\right)}{\partial \mathbf{F}} = [\det \mathbf{F}]^{-1/3}\,\mathbb{K} : \frac{\partial \Psi_{\text{iso}}\left(\overline{\mathbf{F}}\right)}{\partial \overline{\mathbf{F}}} = [\det \mathbf{F}]^{-1/3}\,\mathbb{K} : G\,\overline{\mathbf{F}}\left[1 + \frac{b}{n}\left[\mathbf{I} : \left[\overline{\mathbf{F}}^{\mathrm{T}} \cdot \overline{\mathbf{F}}\right] - 3\right]\right]^{n-1}, \tag{7}$$

with the fourth-order projection tensor $\mathbb{K} = \mathbb{I} - \frac{1}{3}\mathbf{F}^{-\mathrm{T}} \otimes \mathbf{F}$, and the volumetric contribution,

$$\mathbf{P}_{\text{vol}} = \frac{\partial \Psi_{\text{vol}}(\mathbf{F})}{\partial \mathbf{F}} = \det \mathbf{F}\,\frac{\partial \Psi_{\text{vol}}(\mathbf{F})}{\partial \det \mathbf{F}}\mathbf{F}^{-\mathrm{T}} = \kappa\left[[\det \mathbf{F}]^2 - \det \mathbf{F}\right]\mathbf{F}^{-\mathrm{T}}. \tag{8}$$

### 3.2. Material motion problem: Kinematics & Eshelby stress

Configurational mechanics lies in the reformulation of the kinematics and projection of the balance equations to the material manifold. The definition of the Eshelby energy–momentum tensor[4] in the material motion description is in the heart of the theory. In this alternative kinematic approach, the coordinates in the material configuration ($\mathbf{X}$) are mapped from the coordinates in the spatial configuration ($\mathbf{x}$) as $\mathbf{X} = \boldsymbol{\phi}(\mathbf{x})$. Consequently, the inverse deformation gradient is defined as $\mathbf{f} = \nabla \boldsymbol{\phi}(\mathbf{x})$, with $\nabla$ the gradient operator in the spatial configuration. Fig. 5 illustrates the material motion kinematic description.

**Remark.** The direct and inverse deformation gradient are related as $\mathbf{F}^{-1} = \mathbf{f} \circ \boldsymbol{\varphi}(\mathbf{X})$ and $\mathbf{f}^{-1} = \mathbf{F} \circ \boldsymbol{\phi}(\mathbf{x})$, where $\circ$ denotes the composition operation. □

Akin to the energy density $\Psi(\mathbf{F}; \mathbf{X})$ defined in $\Omega_0$, an energy density $\psi = \psi(\mathbf{f}, \boldsymbol{\phi})$ can be re-defined per unit volume in $\Omega$, so that $\Psi \simeq [\det \mathbf{F}]\,\psi$. This new energy density serves as a potential for the Eshelby stress tensor (Eshelby, 1951; Kienzler and Herrmann, 1997) in the material configuration through a push-back operation,

$$\boldsymbol{\Sigma}(\mathbf{f}) = \frac{\partial \psi(\mathbf{f})}{\partial \mathbf{f}} \cdot \left[\operatorname{cof} \mathbf{f}\right]^{-1}, \tag{9}$$

with $\operatorname{cof} \mathbf{f} = [\det \mathbf{f}]\,\mathbf{f}^{-\mathrm{T}}$ the cofactor of the reverse deformation gradient.

[4] Different derivations of the Eshelby stress tensor, also known as energy–momentum tensor, are given in literature (see, e.g., Eshelby (1975), Braun (1997)).

Furthermore, the stress tensor can be reformulated in the form of the Eshelby energy–momentum tensor (Eshelby, 1975) as a function of the direct deformation gradient

$$\boldsymbol{\Sigma}(\mathbf{F}) = \Psi \mathbf{I} - \mathbf{F}^{\mathrm{T}} \cdot \frac{\partial \Psi}{\partial \mathbf{F}}. \tag{10}$$

The energy–momentum tensor in Eq. (10) allows to calculate the Eshelby stress via post processing based on the solution of the spatial motion problem.

### 3.3. Numerical aspects: The configurational force method

The material motion problem can be discretized via FE to obtain configurational forces at the nodes of the discretization by elements in $\mathcal{B}_{\mathrm{e}} \in \Omega_0$ (Steinmann et al., 2001). The configurational force at global node $A$ can be calculated using the material gradient of the global node $A$ basis function ($N^A$), the Eshelby stress tensor ($\boldsymbol{\Sigma}$), and the FE assembly operator $\mathop{\mathbf{A}}_{e=1}^{n_{\mathrm{el}}}$ over all elements

$$\mathbf{F}^A_{\mathrm{CNF}} = \mathop{\mathbf{A}}_{e=1}^{n_{\mathrm{el}}} \int_{\mathcal{B}_{\mathrm{e}}} \boldsymbol{\Sigma} \cdot \nabla_0 N^A \mathrm{dV}. \tag{11}$$

The physical meaning of the Eshelby stress in Eq. (10) can be further discussed (Eshelby, 1999). Overall, configurational forces are associated with the tendency of an elastic structure to undergo a change in its material configuration, leading to alterations in its potential energy. A number of variational frameworks have been proposed to explain the physical sense of configurational forces acting on material inhomogeneities. Among others, the seminal one by Strifors (1974) and the recent one by Schmitz and Ricoeur (2023) can be consulted. In an arbitrary part of a body containing a crack that $\alpha$ that undergoes a virtual extension $\delta^\alpha$, let $\mathbf{F}^\alpha_{\mathrm{CNF}}$ be a configurational force acting on the defect. As a consequence of the variational setting, the structure reduces its potential energy by $\mathbf{F}^\alpha_{\mathrm{CNF}} \cdot \delta^\alpha$, which is the virtual work done by the configurational force at the defect. This work is equal to the reduction of the total potential energy (dissipation) originated by the virtual crack extension. The variational energy balance is set as the difference between the decrement of the internal energy density and the reversible virtual work for the virtual extension $\delta^\alpha$. From this energy balance, the Eshelby stress tensor can be extracted in its energy–momentum tensor representation.

The numerical features of the spatial FE discretization play a major role. Since a FE scheme is itself an approximation to the continuum setting, spurious configurational forces may arise on nodes at the contour and inside the bulk material. To mitigate such inaccuracies, the FE spatial discretization needs to be fine enough (Rohracker et al., 2023). Furthermore, the nature of the basis functions utilized for the Galerkin discretization affect the accuracy of the method. In the present work, we employ continuous piecewise quadratic polynomials, which provide a better approach than linear ones. The open source FE suite FEniCS with the NonLinearVariationalProblem (Logg et al., 2012) is used to solve the BVPs. The description of the bespoke BVPs to be solved will be completed in the following sections.

## 4. LEFM crack tip analytical solutions on Pacman-shaped domains

We begin with a preliminary theoretical and numerical approach to assess the effectiveness of the configurational force method in determining the $J$-integral. The strategy is rooted in the well-established LEFM crack tip solutions applied up to the finite strain regime. Moreover, we opt for a three-dimensional implementation to emulate the nearly plane stress conditions in the thin experimental samples.[5] Within this context, we introduce a BVP based on Pacman-shaped domains that reproduce the crack tip vicinity. The outer circumferential surface of the domains is subjected to displacement boundary conditions according to the LEFM crack tip solution, which is parametrized in terms of the $J$-integral. Subsequently, the displacement field inside the crack tip domain is solved via the FE method and the nodal configurational forces are calculated with the post-processing algorithm detailed in Section 3.2. Then we sum the configurational forces acting on the nodes at the crack front and calculate the force per unit thickness. The resultant value can be benchmarked against the value of $J$ prescribed to deform the Pacman-shaped domain.

### 4.1. J-Controlled displacement prescribed on external contour

The mode-I plane stress LEFM solution for the crack tip displacement field is a function of polar coordinates: radius ($r$) and angle ($\theta$), with origin the crack tip, defined in the material configuration (see Fig. 6c for an illustration of the reference frame).

The horizontal ($u_{\mathrm{x}}$) and vertical ($u_{\mathrm{y}}$) displacement fields in terms of $J$ read

$$u_{\mathrm{x}} = \sqrt{\frac{J\,[1+\nu]}{G\pi\,[1-\nu^2]}}\sqrt{r}\cos\frac{\theta}{2}\left[\frac{4}{3}-\cos^2\frac{\theta}{2}\right] \quad \text{and} \quad u_{\mathrm{y}} = \sqrt{\frac{J\,[1+\nu]}{G\pi\,[1-\nu^2]}}\sqrt{r}\sin\frac{\theta}{2}\left[\frac{4}{3}-\cos^2\frac{\theta}{2}\right], \tag{12}$$

[5] Note that the implementation of the plane strain condition has been explored with a simplified 2D implementation by Steinmann (2022).

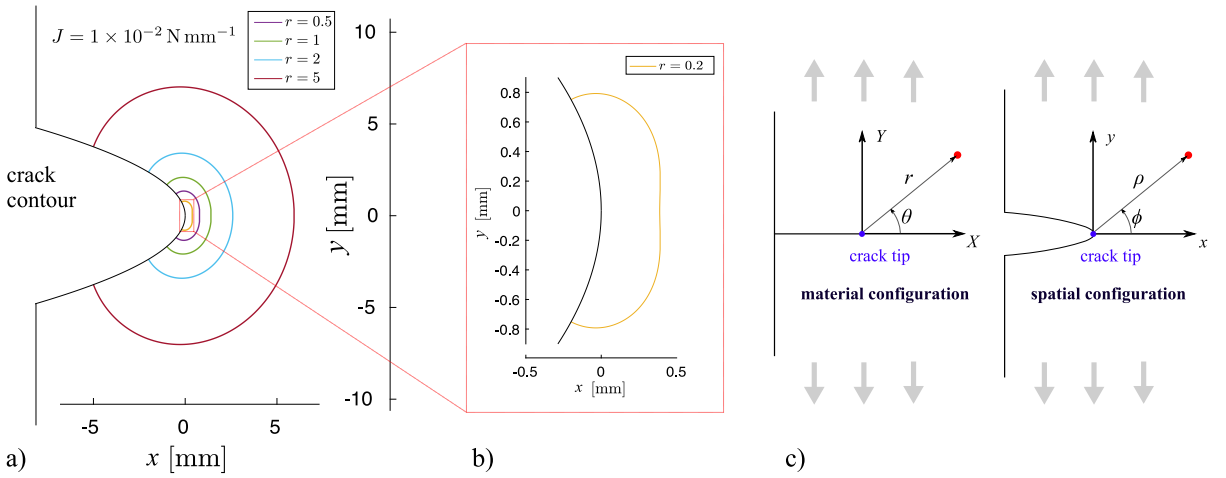


**Fig. 6. External contours of Pacman-shaped domains replicating the crack tip vicinity after deformation according to LEFM displacement solution for a number of radial coordinates.** (a) Contours for plane stress deformation hypothesis for radial coordinates $r = \{0.5, 1, 2, 5, 10\}$ mm and (b) detail on the small coordinate $r = 0.2$ mm. The contours adopt a lobe-like shape as the radius decreases. (c) Cartesian and polar coordinates referred to the material configuration. A same value of $J = 1 \times 10^{-2}\,\mathrm{N\,mm^{-1}}$ is used.

where the constitutive parameters are the small strain shear modulus ($G$) and the Poisson ratio ($\nu$). Note that this solution arises in the spirit of the neo-Hookean constitutive model restricted to small strains and under mode-I loading. In order to use meaningful constitutive values, we make again a reference to Appendix A to take $G = 3\,\mathrm{kPa}$ and $\kappa = 100\,\mathrm{kPa}$.[6]

Upon examining the LEFM solution, it becomes evident that the radial coordinate is subjected to the well-known square-root dependence. Next, let us define circular domains of radii ($r$) 0.2 , 0.5 , 1 , 2 , and 5 , and map them by the displacements in Eq. (12) to the spatial configuration. Note that the shape of a deformed contour is not solely contingent on the magnitude of $J$ but also on the value of $r$. Fig. 6 provides a visual representation of various contours for radii ranging from 0.2 mm to 5 mm. The contours illustrate the large extent of crack opening in spite of a small loading determined by $J = 1 \times 10^{-2}\,\mathrm{N\,mm^{-1}}$. All these profiles will be employed in the following section to set the boundary conditions on the FE Pacman-shaped domains.

### 4.2. Configurational forces versus prescribed $J$-integral

Tensile (mode-I) loading of a structure with a crack leads to the progressive deformation of the crack tip and the subsequent increase of $J$. In our FE framework, increasing values of $J$ are taken as the input to control the deformation of Pacman-shaped domains with radii $r = \{0.2, 0.5, 1, 2, 5\}$ mm and respective thicknesses of $t = \{0.1, 0.25, 0.5, 1, 2.5\}$ mm. The FE model is solved on the same mesh, where the nodal coordinates are scaled according to the radius.[7] The 3D mesh comprises 34 823 tetrahedral elements and benefits from double symmetry in the $x$–$z$ plane at the crack and $x$–$y$ plane at half the thickness to reduce the computational domain to one fourth of the total Pacman-shaped domain.[8] Note that the calculation of nodal forces on the symmetry planes is consistently performed in accordance with symmetry arguments. Besides, the mesh is refined with an element size half the size in a cylindrical region centered at the crack tip with half the radius of the mesh. The loading is performed as a line ramp with incremental values of $J$ ranging from zero to $1 \times 10^{-2}\,\mathrm{N\,mm^{-1}}$. Fig. 7 contains a representative Pacman-shaped domain for $r = 1$ mm and $t = 0.5$ mm after deformation on which the nodal configurational forces are illustrated with vectors. We depict the results for three loading stages corresponding to three values of $J$: $1 \times 10^{-6}\,\mathrm{N\,mm^{-1}}$, $1 \times 10^{-4}\,\mathrm{N\,mm^{-1}}$, and $1 \times 10^{-3}\,\mathrm{N\,mm^{-1}}$. An inspection of the forces at the crack front and its vicinity leads to several observations.

Let us make a distinction between physical and spurious configurational forces. The first ones are those actuating on defects with the ability to drive changes in the material configuration. The last ones are nodal forces that actuate on the nodes of the FE mesh as a consequence of the approximated nature of the FE method itself and the spatial discretization, but lack a physical meaning

[6] The Poisson ratio and the bulk modulus are related via $\nu = \frac{3\kappa - 2G}{2[3\kappa + G]}$. For $G = 3\,\mathrm{kPa}$ and $\kappa = 100\,\mathrm{kPa}$, $\nu = 0.485$, which suffices to model nearly incompressible material behavior. Alternatively, the use of a Poisson ratio approaching 0.5 in the limit $J \to 1$ requires proper numerical treatment to alleviate volumetric locking. The Lagrange-multiplier method in two- and three-field variational schemes are customary approaches to eliminate this difficulty (Brezzi and Fortin, 1991; Simo et al., 1985). We have verified that the compressible effects introduced by the use of a lower bulk modulus are negligible and, instead, the model has better numerical performance.

[7] Note that the use of a common mesh prevents numerical variability when comparing the different domains.

[8] As an alternative, 2D simulations would allow the implementation of the plane stress assumption with reduced computational cost. Nevertheless, we believe that 3D simulations can be better motivated by the experimental observations in Section 2 and the actual dimensions of the soft-elastomer samples, specifically the thickness of the samples ($t = 0.5$ mm). In addition, note that double symmetry enables high numerical accuracy with significantly reduced computational times—less than one hour for each simulation.

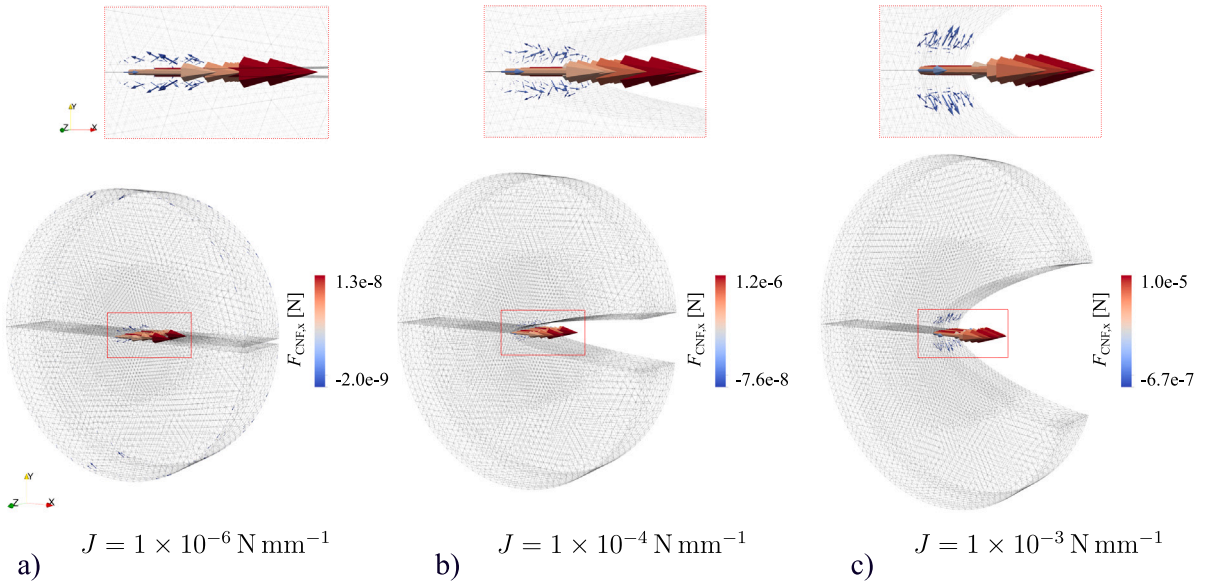


**Fig. 7. Configurational forces in a crack-tip Pacman-shaped domain replicating the crack tip vicinity.** The domain, with radius $r = 1$ mm and thickness $t = 0.5$ mm, is subjected to $J$-controlled displacement boundary conditions on its external (circumferential) contour according to the LEFM analytical solutions. The color of the vectors representing the forces indicate the magnitude of the horizontal component of the force, i.e., $F_{\mathrm{CNF,x}}$. Zoom details of the nodal forces at the crack tip are included. The constitutive model used to solve the deformation of the domain is neo-Hookean, i.e., $n = 1.0$ and $b = 1.0$.

in the continuum mechanical setting. Within this context, only the forces at the crack tip front edge have a physical meaning in terms of driving forces. As it can be noticed from Fig. 7, the presence of spurious forces is more relevant at lower values of $J$. When the loading increases and the crack mouth further opens, the physical configurational forces prevail and the spurious ones are negligible. To get a better approximation of $J$, however, we add up the spurious configurational forces in a region surrounding the crack tip to the crack tip physical forces, as it is described in Denzer et al. (2003).

Each loading step enables two visions: (i) a value of $J$-integral renders the deformation of the crack tip Pacman-shaped domain and (ii) the constitutive response of the domain results in configurational forces at the crack tip. The total configurational force $F_{\mathrm{CNF}}$ can be calculated adding up the forces at the nodes within the evaluation domain, including the crack edge.[9] The division of the total force by the thickness yields the configurational forces per unit thickness, whose magnitude can be compared to $J$ in the spirit of $\mathbf{J} = -\sum_A^C \mathbf{F}^A_{\mathrm{CNF}} / \int_C \mathrm{ds}$ and the configurational dissipation $\mathbf{F}_{\mathrm{CNF}} \cdot \boldsymbol{\delta} \overset{!}{\leqslant} 0$ and $\mathbf{J} \cdot \boldsymbol{\delta} \overset{!}{\geqslant} 0$, with $C$ the number of nodes within the crack tip evaluation domain and $\boldsymbol{\delta}$ and extension of the crack.[10] Note that the integral simplifies to the thickness for a crack front aligned with the thickness direction. This comparison allows to assess the performance of the configurational force method, in such a way that the configurational force is expected to approximate $J$. Provided the limitations of the LEFM solution, one can expect a trustworthy performance only in the small deformation regime. In spite of this theoretical limitation, we extend the analysis to the finite deformation regime.

The results are presented as $F_{\mathrm{CNF}} - J$ curves in Fig. 8a (and detail for small values of $J$ in Fig. 8b) for the contours and radial coordinates introduced in the previous section. Up to a value of $J$ of about $1 \times 10^{-4}\,\mathrm{N\,mm^{-1}}$, the configurational force matches $J$ with a rather small relative error (lesser than 5%) for the domains with radii of 0.2 mm, 0.5 mm, 1 mm, and 2 mm. For the radius of 5 mm, the agreement is quite satisfactory, with the $F_{\mathrm{CNF}}$ curve aligning closely with the diagonal, for which $F_{\mathrm{CNF}} = J$. Note that decreasing radii annul the validity of the Pacman-shaped domains due to the crack tip singularity in the LEFM analytical solution. Furthermore, as shown in Fig. 6, the agreement not only applies to the small deformation regime but extends to significant deformations. This is a quite interesting finding since the prerequisites of asymptotic crack tip fields of LEFM are intuitively expected to be severely violated. However, values of $J$ that are even larger result in more significant disagreements and a larger sensitivity to the radius of the domain.

For the reader interested in the influence of the spurious forces around the crack tip, we have additionally performed the crack tip evaluation of the configurational force in Appendix B. To that end, we present the configurational force solely as the summation of the configurational forces at the crack front edge, i.e., without summing the spurious forces. Fig. B.14 presents the $F_{\mathrm{CNF}} - J$ curves

[9] The y- and z-component of the total configurational force ($F_{\mathrm{CNF,y}}$ and $F_{\mathrm{CNF,z}}$, respectively) vanish due to the symmetry of the loading state (mode-I) and the symmetry of the computational domain. Therefore, the magnitude of the total configurational force ($F_{\mathrm{CNF}}$) is obtained adding up the x-component of the configurational forces on the target nodes. In the following, $F_{\mathrm{CNF,x}}$ will be simplified to $F_{\mathrm{CNF}}$.

[10] The evaluation domain in which the configurational forces are added up to render a total configurational forces is defined for $r \leq 0.5 R_{\mathrm{Pacman}}$, with $R_{\mathrm{Pacman}}$ the radius of the circular domain and $r$ the radial coordinate centered at the crack tip.

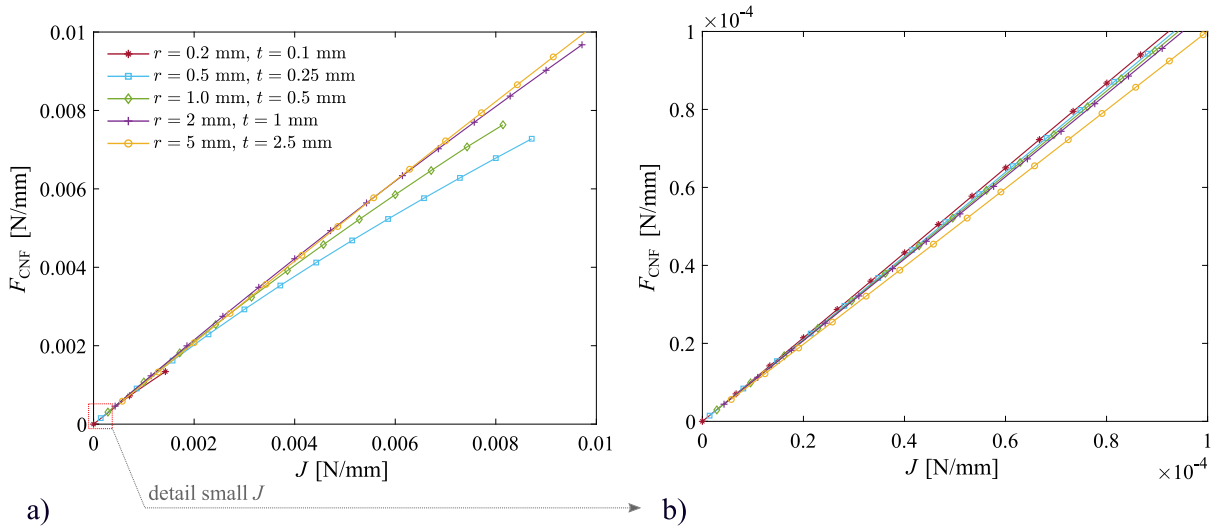


**Fig. 8. Evolution of the total configurational force on the Pacman-shaped domains subjected to $J$-controlled loading.** (a) The evolution of $F_{\text{CNF}}$ is plotted against $J$ for the all the radii and thicknesses utilized to define the Pacman domains: $r = \{0.2, 0.5, 1, 2, 5\}$ mm and $t = \{0.1, 0.25, 0.5, 1, 2.5\}$ mm, respectively for each domain. (b) Detail for small values of $J$. The total force $F_{\text{CNF}}$ is obtained adding up all the nodal forces at the crack edge. In addition, the spurious forces located at $r \leq 0.5R_{\text{Pacman}}$, with $R_{\text{Pacman}}$ the radius of the circular domain and $r$ the radial coordinate centered at the crack tip, are added up to the physical forces at the crack front edge according to the domain evaluation method. The constitutive model is neo-Hookean ($n = 1$, $b = 1$).

for the same array of radii and loading of the Pacman domain. Overall, the tendencies and quantitative behavior of $F_{\text{CNF}}$ resonate with the results in Fig. 8, with slightly lesser values.

The use of Pacman-shaped domains is instructive as a first approach to explore the relationship between configurational forces at the crack tip vicinity and the $J$-integral. Nonetheless, the strategy is subjected to LEFM solutions, which have been applied up to the finite deformation regime. Therefore, as it can be observed in Fig. 8a for large values of $J$, the agreement between $F_{\text{CNF}}$ and $J$ is less precise for larger deformations. This fact motivates a more sophisticated approach to link $F_{\text{CNF}}$ and $J$ at finite strains.

## 5. Configurational forces via comprehensive boundary value problem

While the study of the crack-tip Pacman-shaped domain served as a valuable initial step in establishing a link between configurational forces and the well-established LEFM theory, it falls short of providing a robust connection with the experimental observations. In this section, we take a step forward. Instead of modeling solely the crack tip vicinity, we employ a BVP that replicates the complete geometry of the real sample under tensile loading. This approach, coupled with the use of a more sophisticated constitutive model with strain hardening, brings the deformation at the crack tip vicinity closer to the real samples. On this basis, the configurational force method yields results that are closely representative of the real setting. To validate that the deformation of the crack tip adjoining area replicates the experimental observations with sufficient accuracy, we calculate the error between the numerical and experimental displacements.

### 5.1. Virtual experiment

A more robust connection between experimentation and configurational forces requires solving via the FE method a BVP that models a rectangular sample with a pre-cut subjected to tensile loading.[11] The FE mesh mimics the geometry of the samples introduced in Section 2. The length of the virtual sample is 30 mm, i.e., the initial distance between the clamps in the experimental setting. In addition, a discontinuity in the middle region of the mesh allows to reproduce the pre-cuts and the initially sharp crack tip. Five meshes are created with a number of tetrahedral elements of 25 282, 29 786, 33 913, 39 328, and 42 239, respectively for the crack-width ratios ($c/w$) from 0.1 to 0.5, and benefiting from symmetry in the $x$–$z$ plane at the crack and $x$–$y$ plane at half the thickness to reduce the computational domain to one fourth of the total sample. These different values owe to the different ways in which the mesh refinement around the crack tip is done: a box 0.5 mm above and below the crack and with a margin of 1 mm to the crack tip with elements times 0.25 the size of the outer elements. A FE solution scheme akin to the one used to solve the Pacman-domain computations is implemented. Here, however, the GNH model with a strain hardening exponent is calibrated and used to better capture the material behavior.

[11] We refer to the *in silico* framework that reproduces the experimental setting and sample as "virtual experiment" and "virtual sample".

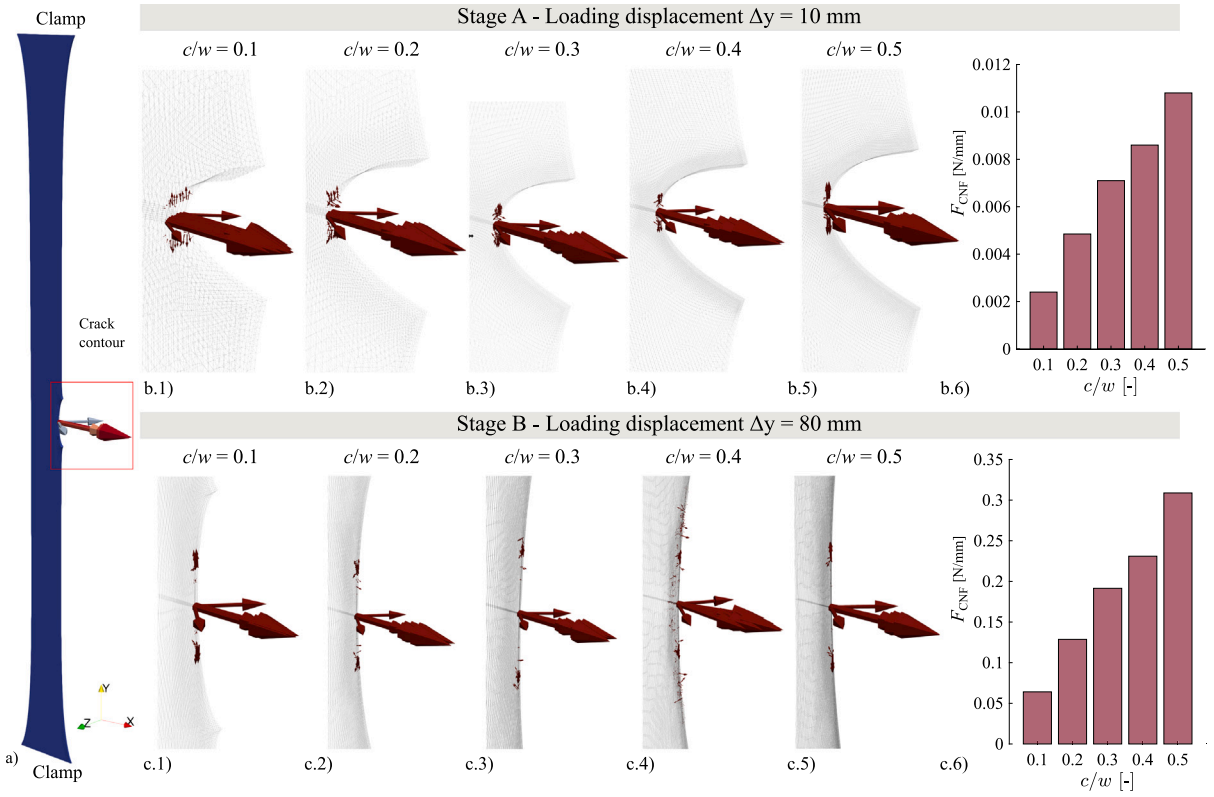


**Fig. 9. Nodal configurational forces at the crack tip vicinity on virtual rectangular samples featuring pre-cuts.** The implementation replicates the experimental samples and the testing tensile loading setup. (a) Virtual sample after deformation including the vector configurational forces at the nodes of the FE mesh, which are prominent at the crack front. (b.1-5) Detail of the configurational forces at the crack contour in virtual samples featuring pre-cuts of different lengths and a same total displacement of the clamps of $\Delta y = 10$ mm and (c.1-5) $\Delta y = 80$ mm. The arrows representing the nodal configurational forces are scaled to render similar visual dimensions, with scale factors of 1, 1.7, 2.4, 3.1, and 3.8, respectively for $c/w$ from 0.5 to 0.1 (b.6) Total configurational forces per unit thickness for all the crack-width ratios and a same total displacement of the clamps of $\Delta y = 10$ mm and (c.6) $\Delta y = 80$ mm.

As for the Pacman-shaped crack tip domains, the largest configurational forces manifest at the crack front. To illustrate this result, Fig. 9a provides a visual representation of the configurational forces on a virtual sample undergoing tensile deformation. To dig further into this behavior, Fig. 9 showcases the crack contour and crack tip vicinity for the different crack-width ratios. Two loading stages, i.e., displacement of the clamps, are chosen to explore the forces at two stages of deformation of the crack contour: Stage A of 10 mm and Stage B of 80 mm. In accordance with the earlier distinction of physical and spurious configurational forces, these illustrations display nearly negligible spurious forces and, consequently, emphasize the prevalence of physical forces. A visual inspection reveals the presence of only minor vertical spurious forces in the nodes adjacent to the crack front.

A matter of interest is the comparison of the configurational forces across the array of crack-width ratios while maintaining the same displacement of the clamps. The reader may note that the arrows representing the nodal configurational forces are scaled and do not maintain the proportion between the different cases for each crack-width ratio. Moreover, and unless the number of nodes in the thickness direction is the same, the comparison of individual nodal forces is meaningless. A sound comparison requires the calculation of the total configurational force by adding up all the nodal forces at the crack front and then dividing the resulting value by the thickness of the sample. The bar-plots in Figs. 9b.6 and c.6 contain the results for all the crack-width ratios and the respective loading stages. For the same displacement of the clamp, the magnitude of the configurational force increases by more than a 350% from the shortest pre-cut ($c/w = 0.1$) to the largest one ($c/w = 0.5$). The values of $F_{\mathrm{CNF}}$ for $c/w$ values from to 0.1 to 0.5, respectively, and loading Stage A are $2.4 \times 10^{-3}\,\mathrm{N\,mm^{-1}}$, $4.9 \times 10^{-3}\,\mathrm{N\,mm^{-1}}$, $7.1 \times 10^{-3}\,\mathrm{N\,mm^{-1}}$, $8.6 \times 10^{-3}\,\mathrm{N\,mm^{-1}}$, and $10.8 \times 10^{-3}\,\mathrm{N\,mm^{-1}}$. For the loading Stage B, $F_{\mathrm{CNF}}$ is $0.064\,\mathrm{N\,mm^{-1}}$, $0.129\,\mathrm{N\,mm^{-1}}$, $0.192\,\mathrm{N\,mm^{-1}}$, $0.231\,\mathrm{N\,mm^{-1}}$, and $0.309\,\mathrm{N\,mm^{-1}}$. Akin to stress intensity factors for stress evaluation in LEFM, the crack tip configurational force increases with strain concentration, here with the crack length.

An alternative insightful way to present the results involves plotting the evolution of the crack front configurational force as a function of the clamp displacement. These plots are included in Fig. 10 as $F_{\mathrm{CNF}}$–displacement curves for displacement values from

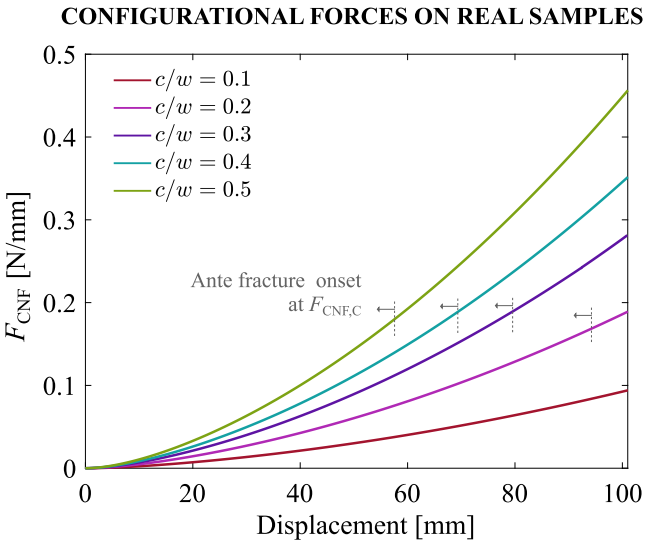


**Fig. 10. Configurational force at the crack tip as a function of the displacement of the clamps.** The results cover all the crack-width ratios: $c/w = \{0.1, 0.2, 0.3, 0.4, 0.5\}$. In addition, the displacement for crack onset is estimated from Fig. 2 for each crack-width ratio and indicated with an arrow. The values of $F_{\mathrm{CNF}}$ associated to fracture onset denote the material inherent critical value for fracture onset, $F_{\mathrm{CNF,C}}$.

zero to the maximum displacement admissible before crack onset.[12] As it can be observed, for a same loading stage, larger crack lengths produce a more intense stress concentration, hence larger values of the configurational force. For an illustrative displacement of 40 mm, and respectively for the crack-width ratios from 0.1 to 0.5, the configurational force is $0.021\,\mathrm{N\,mm^{-1}}$, $0.043\,\mathrm{N\,mm^{-1}}$, $0.063\,\mathrm{N\,mm^{-1}}$, $0.078\,\mathrm{N\,mm^{-1}}$, and $0.100\,\mathrm{N\,mm^{-1}}$.

The curves depicting the crack tip configurational force and the displacement at fracture observed experimentally allow to deduce a critical value of the configurational force for fracture onset. The evolution of the crack tip configurational force is dependent on the boundary conditions, namely the loading state and severity of the material inhomogeneity, akin to classical strength evaluation via, e.g., stress intensity factors. The critical configurational force for fracture onset, denoted here as $F_{\mathrm{CNF,C}}$, is, however, material inherent and does not depend on geometry, stress state, and loading condition. If we leverage the $F_{\mathrm{CNF}}$ curves and annotate the displacement for fracture onset, a same material inherent ($c/w$-independent) $F_{\mathrm{CNF,C}}$ value is expected. As it can be appreciated in Fig. 10, fracture onset occurs along the different crack-width ratios for a convincingly similar value of the configurational force of $0.19\,\mathrm{N\,mm^{-1}}$, where the small scatter owes to the experimental variability to determine the displacement for fracture onset. This is a key point enabling the use of nodal configurational forces for strength evaluation in fracture criteria.

### *5.2. Experimental validation of the crack tip displacement fields*

The deformation in the crack tip vicinity is complex and cannot be solely determined through calibration based on tensile tests performed on uncut, bulk samples. However, a good reproduction of the crack adjoining area is paramount to render reliable values of $J$. To assess the quality of our constitutive model, next we explore the error between the numerical and experimental surface displacement fields. To do that, we calculate the absolute error between the fields within a region of interest around the crack tip. The results, which are presented in Fig. 11 for the undeformed (material) and deformed (spatial) configurations, pertain to the vertical and horizontal fields. To enable comparisons between different crack-width ratios, we normalize the error measure by dividing it by the grip displacement. As observed, the error remains below 2% for crack-width ratios of 0.1 and 0.2, and below 10% for all cases. Equally important is the fact that the error does not increase in the vicinity of the crack tip, indicating a satisfactory level of accuracy in this complex area. The areas where the error increases can be justified by the choice of the GNH constitutive model and the fact that the material does not perfectly adjust to this constitutive assumption.

## 6. Validation of $J$-integral via finite strain analytical solution

The bespoke BVP introduced in the previous section successfully reproduces the experimental observations on the soft elastomer samples. This is a prerequisite for applying the configurational force method to approximate $J$. In the following, we present a further validation based on an alternative estimation of $J$ with a finite strain analytical crack tip solution.

[12] The numerical BVP does not model crack propagation. Instead, the displacement value that produces fracture onset is identified from the experimental results.

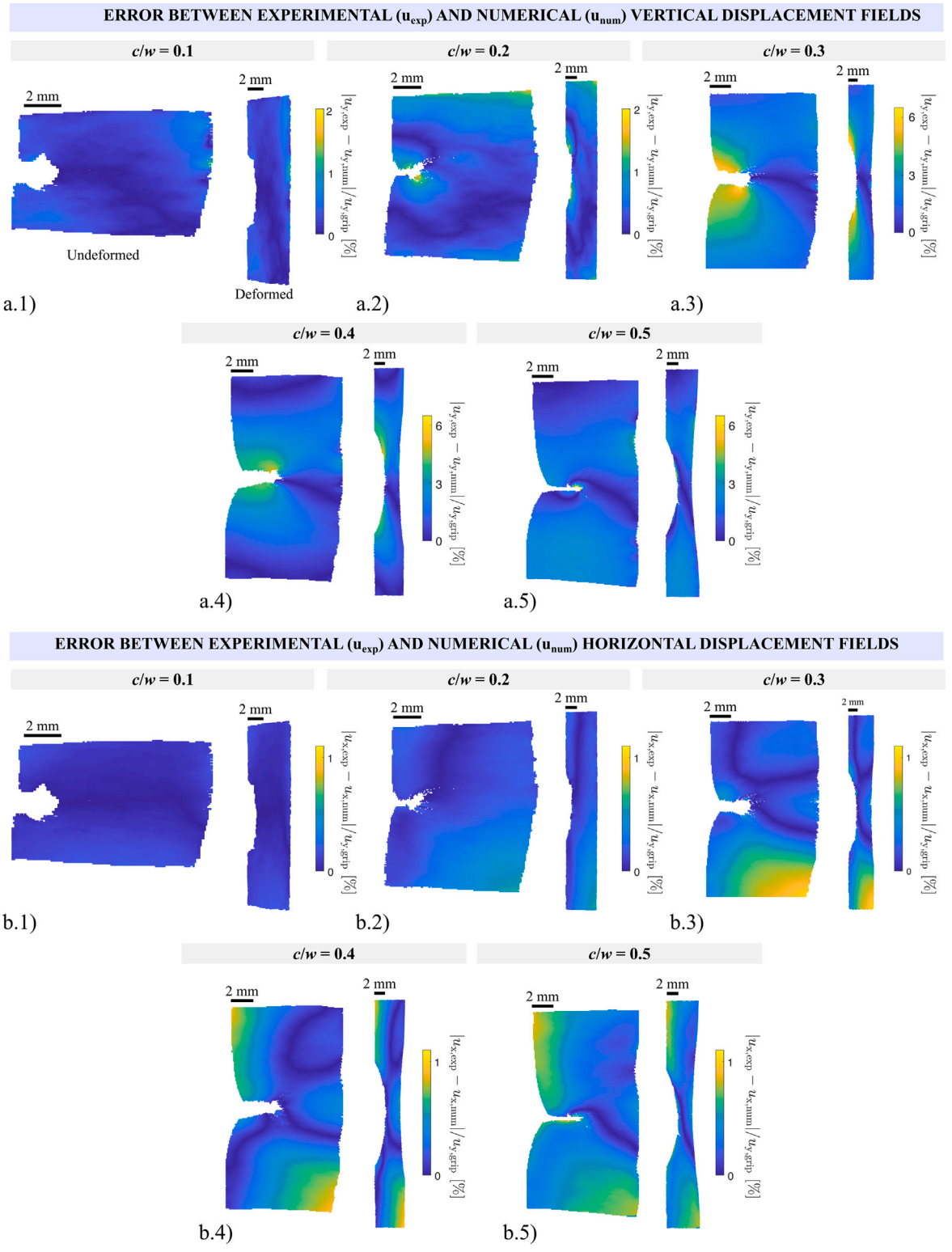


**Fig. 11. Error between the experimental and numerical, vertical and horizontal, displacement fields at the crack tip vicinity.** The absolute error between the fields is calculated for each spatial position in the undeformed and deformed configurations for the crack-width ratios $c/w = \{0.1, 0.2, 0.3, 0.4, 0.5\}$. The error is divided by the vertical displacement of the grips ($u_{y,grip}$) for the respective crack-width ratios ante fracture onset, i.e., 80 mm, 70 mm, 62 mm, 53 mm, and 43 mm.

In a similar manner that the LEFM close-form expressions relate the displacement field at the crack tip vicinity to the stress intensity factors and $J$-integral (see previous Section 4), Long et al. (2011), Long and Hui (2015) proposed analytical solutions to define the coordinates of the crack contour after finite strain mode-I deformation and accounting for strain hardening/softening. Such relations allow to estimate $J$ by fitting the vertical displacement field, following a similar approach as described in Moreno-Mateos et al. (2023b). Here, this strategy will be used to determine values of $J$ from the crack tip displacement fields solved in the virtual experiments (Section 5.1). Subsequently, these values will be compared to the configurational forces.

The crack tip solution postulates that the deformed coordinates in the crack tip vicinity where $r \to 0$ are a series of functions of the polar coordinates in the material configuration. This allows to mimic the crack tip blunting that occurs in elastomers in the large deformation regime (Spagnoli et al., 2023). The analytical solution can be particularized to yield the bespoke vertical displacement field for a GNH material as

$$u_{\mathrm{y}} = a r^{1-\frac{1}{2n}} U(\theta, n), \tag{13}$$

with $U(\theta, n)$ a function that depends on the angular polar coordinate at the material configuration and the strain hardening/softening coefficient $(n)$,

$$U(\theta, n) = \sin(\theta/2) \sqrt{1 - \frac{2\xi^2 \cos^2(\theta/2)}{1 + \omega(\theta, n)}} \left[\omega(\theta, n) + \xi \cos(\theta)\right]^{\xi/2}, \tag{14}$$

for $\xi = 1 - \frac{1}{n}$ and $\omega(\theta, n) = \sqrt{1 - \xi^2 \sin^2(\theta)}$.

The parameter $a$ in Eq. (13) is a positive amplitude that can be expressed in terms of $J$. Thus, the vertical displacement field can be expressed as a function of $J$.[13] In turn, the constitutive parameters of the GNH model for the FE simulations and the analytical model are the same ones, i.e., $G = 3\,\mathrm{kPa}$, $n = 1.05$, and $b = 1.05$, as detailed in Appendix A. Note that the shear and bulk moduli are the same as those used for the LEFM Pacman-shaped domain simulations in Section 4. According to the reduced thickness of the VHB samples, the plane stress assumption renders

$$a = \left[ J \left[\frac{2}{G\pi}\right] \left[\frac{n}{b}\right]^{n-1} \left[\frac{2n}{2n-1}\right]^{2n-1} n^{n-1} \right]^{\frac{1}{2n}}. \tag{15}$$

Next, let us define a least squares minimization problem to fit the analytical solution for the vertical $J$-controlled displacement field $(u_{\mathrm{y,ana}})$ to a numerical displacement field $(u_{\mathrm{y,num}})$. The fitting is done at $i \in s$ points in an annular grid, i.e.,

$$\min_{J \in \mathbb{R}^+} \sum_{i}^{s} \left[ u_{\mathrm{y,ana}}^{2n} - u_{\mathrm{y,num}}^{2n} \right]_i^2. \tag{16}$$

**Remark.** The exponent $2n$ used with the displacements in Eq. (16) is due to the potential dependence of $J$ on the exponent $n$ as defined in Eq. (15). □

Contrary to the DIC displacement fields where each displacement value corresponds to a pixel in a structured grid, the spatial location of the nodal displacements in the FE field corresponds to the nodes of the FE mesh. To enable the calculation in Eq. (16) according to fitting points located in a structured grid, the numerical displacement fields are interpolated to a new mesh in which the new nodes form a equi-spaced rectangular grid. These new nodal positions mimic the same 0.07 mm/pixel relation as in the DIC images. On these fields, an annular grid is used to calculate $J$. The grid is centered at the crack tip, with final angle of 135° and radius of 17 pixel.

The results reveal a quite satisfactory performance of the framework: $F_{\mathrm{CNF}}$ matches with a great degree of accuracy the estimations of $J$ done on the numerical displacement fields. Fig. 12 illustrates the comparison as well as the annular grids used for the fitting. Nine values of $J$ for equi-spaced displacements, up to a maximum displacement of 80 mm, are plotted together with the $F_{\mathrm{CNF}}$ curves. To quantify the goodness of the agreement, a number of quantitative values of both $F_{\mathrm{CNF}}$ and $J$ are provided in Table 1 for the nine displacement values. The relative error between both quantities is smaller than 42% for all the cases and is convincingly small for increasing displacements, with errors below 10% for a displacement of 80 mm. Sources of error may be due to the boundary conditions of the FE BVP, which does not exactly replicate the ideal plane stress conditions of the analytical solution. Nonetheless, and as indicated previously, the lack of a $J$-dependent solution akin to Eq. (13) for the horizontal crack tip displacement makes Pacman-shaped domain simulations debatable. In summary, the satisfactory agreement between $F_{\mathrm{CNF}}$ and the estimations of $J$ confirms that the configurational force method is able to approximate $J$ at finite strains and for all the lengths of the pre-cuts. This also proves accuracy of the FE solution per se.

For readers interested in the agreement between the analytical solution and the experimental displacement field, Fig. C.15 provides an additional validation of the configurational forces based on the estimation of $J$ directly from the experimental DIC results. The comparison is analogous to the one presented in the current section, but the analytical solution is applied to the experimental vertical displacement fields instead of the numerical ones. Due to factors such as the challenge in identifying the crack tip and the imperfect constitutive behavior as a GNH material, this comparison is less ideal and is subject to additional sources of error. In spite of that, the degree of agreement between $F_{\mathrm{CNF}}$ and $J$ is reasonably good.

[13] The finite strain analytical solution establishes a direct relationship to $J$ only for the vertical crack tip displacement field $(u_{\mathrm{y}})$ and not for the horizontal displacement field $(u_{\mathrm{x}})$. Instead, the horizontal displacement needs to be numerically determined by solving a two-point boundary value problem, as described in Geubelle and Knauss (1994), Long and Hui (2015).

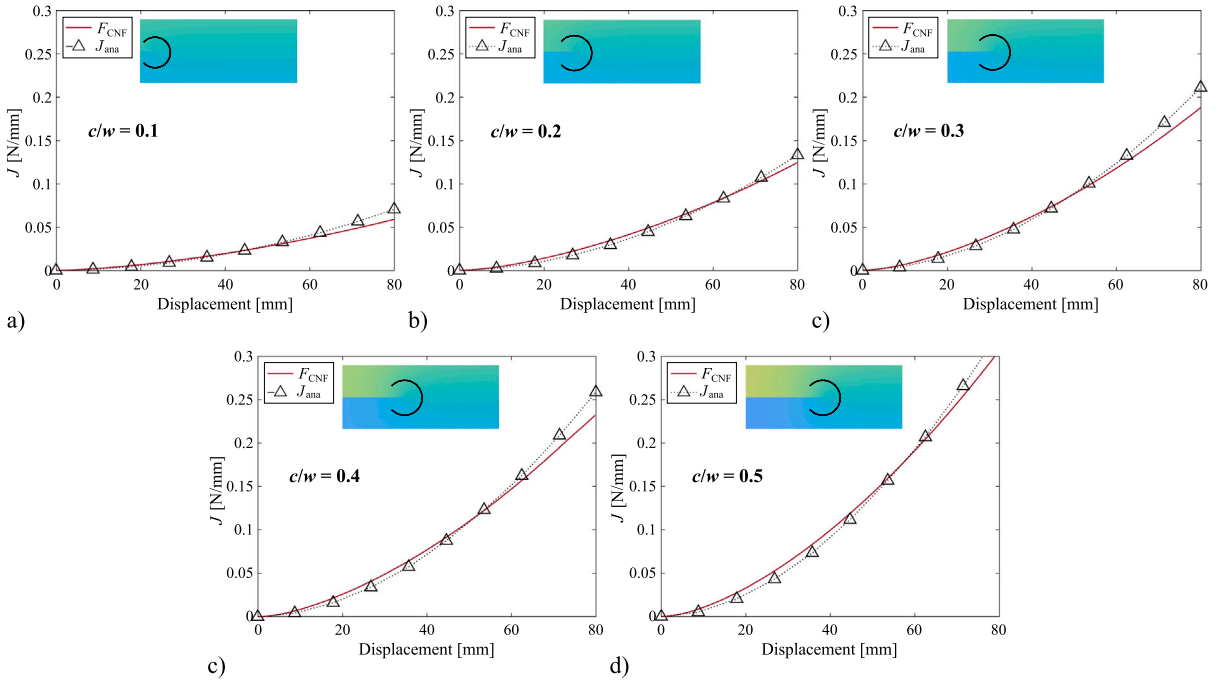


**Fig. 12. Results for $J$-integral estimated from numerical displacement fields and comparison with configurational forces.** The displacement fields used to fit $J$ ($J_{ana}$ in the spirit of the analytical model) are extracted from the FE simulations that implement the virtual tensile experiment to calculate the configurational forces. An annular grid sufficiently close to the crack tip is used for the fitting and depicted with black points. The performance of the configurational force ($F_{CNF}$) to replicate the $J$-integral is validated for the different crack-width ratios $c/w$: (a) 0.1, (b) 0.2, (c) 0.3, (d) 0.4, and (e) 0.5, and for nine displacement points (triangle markers).

**Table 1**
Quantitative summary of the configurational forces ($F_{CNF}$) and the $J$-integral estimated from the displacement fields solved in the virtual experiments. Values are extracted from Fig. 12 for a discrete number of displacements (nine equi-spaced values) during the loading event and spanning all crack-width ratios from 0.1 to 0.5. The relative error between $F_{CNF}$ and $J_{ana}$ is included for each pair of data.

| $c/w$ | Variable | Displacement [mm] | | | | | | | | |
|---|---|---|---|---|---|---|---|---|---|---|
| [–] | | 8.7 | 17.8 | 26.8 | 35.7 | 44.6 | 53.6 | 62.5 | 71.4 | 80 |
| 0.1 | $F_{CNF}$ [N mm$^{-1}$] | 0.0019 | 0.0059 | 0.0113 | 0.0178 | 0.0251 | 0.0336 | 0.0430 | 0.0533 | 0.0641 |
| | $J_{ana}$ [N mm$^{-1}$] | 0.0011 | 0.0042 | 0.0088 | 0.0149 | 0.0228 | 0.0324 | 0.0432 | 0.0562 | 0.0702 |
| | $[F_{CNF} - J]/F_{CNF}$ [–] | 0.42 | 0.29 | 0.22 | 0.16 | 0.09 | 0.04 | −0.00 | −0.05 | −0.10 |
| 0.2 | $F_{CNF}$ [N mm$^{-1}$] | 0.0038 | 0.0121 | 0.0229 | 0.0357 | 0.0508 | 0.0675 | 0.0866 | 0.1071 | 0.1287 |
| | $J_{ana}$ [N mm$^{-1}$] | 0.0022 | 0.0083 | 0.0173 | 0.0291 | 0.0443 | 0.0624 | 0.0826 | 0.1066 | 0.1325 |
| | $[F_{CNF} - J]/F_{CNF}$ [–] | 0.42 | 0.31 | 0.24 | 0.18 | 0.13 | 0.08 | 0.05 | 0.00 | −0.03 |
| 0.3 | $F_{CNF}$ [N mm$^{-1}$] | 0.0056 | 0.0178 | 0.0339 | 0.0528 | 0.0754 | 0.1002 | 0.1287 | 0.1592 | 0.1915 |
| | $J_{ana}$ [N mm$^{-1}$] | 0.0036 | 0.0135 | 0.0280 | 0.0470 | 0.0713 | 0.1000 | 0.1320 | 0.1697 | 0.2103 |
| | $[F_{CNF} - J]/F_{CNF}$ [–] | 0.36 | 0.24 | 0.17 | 0.11 | 0.05 | 0.00 | −0.03 | −0.07 | −0.10 |
| 0.4 | $F_{CNF}$ [N mm$^{-1}$] | 0.0068 | 0.0217 | 0.0417 | 0.0651 | 0.0931 | 0.1240 | 0.1595 | 0.1975 | 0.2310 |
| | $J_{ana}$ [N mm$^{-1}$] | 0.0042 | 0.0161 | 0.0340 | 0.0574 | 0.0875 | 0.1230 | 0.1623 | 0.2086 | 0.2583 |
| | $[F_{CNF} - J]/F_{CNF}$ [–] | 0.38 | 0.26 | 0.18 | 0.12 | 0.06 | 0.01 | −0.02 | −0.06 | −0.1 |
| 0.5 | $F_{CNF}$ [N mm$^{-1}$] | 0.0085 | 0.0275 | 0.0531 | 0.0836 | 0.1200 | 0.1603 | 0.2066 | 0.2563 | 0.3088 |
| | $J_{ana}$ [N mm$^{-1}$] | 0.0052 | 0.0203 | 0.0430 | 0.0731 | 0.1113 | 0.1565 | 0.2064 | 0.2651 | 0.3280 |
| | $[F_{CNF} - J]/F_{CNF}$ [–] | 0.39 | 0.26 | 0.19 | 0.13 | 0.07 | 0.02 | 0.00 | −0.03 | −0.06 |

## 7. Discussion and outlook

### 7.1. Discussion

In the scope of this article, we have assessed the performance of the configurational force method against the fracture mechanics $J$-integral. We have endeavored to merge the numerical setting with experiments conducted on a soft acrylic elastomer. Through this integration, we validate the magnitude of the crack tip configurational force on samples with varying pre-cut lengths, under finite deformations, and prior to crack propagation.

As an instructive preliminary approach, we calculate the configurational forces on Pacman-shaped domains that replicate the crack tip vicinity. These circular domains were deformed according to the LEFM solutions for the crack tip displacement fields, allowing parametrization in terms of the $J$-integral. Notably, the domains were modeled in three dimensions with reduced thickness to approximate the plane-stress-like deformation conditions in the real samples. From theoretical arguments, the total configurational force at the crack tip renders the $J$-integral as a vectorial quantity: its magnitude relates to the traditional scalar $J$-integral and its direction predicts the direction in which the crack propagates. In this regard, a seminal work is due to Strifors (1974), who set a variational statement at crack inhomogeneities to define a crack extension force. The variational framework not only was able to predict crack initiation but also the direction of preferred growth. The crack deflection criterion included the $J$-integral by Rice (1968) as a special case. The reader can notice from Figs. 7 and 9 that the configurational force points in the opposite direction of crack growth, which is a consequence of the derivation of the weak formulation adopted in this work. This setting can be circumvented if the weak formulation is derived from a variational energy balance as outlined by Schmitz and Ricoeur (2023). The $F_{\mathrm{CNF}} - J$ comparison for a number of radii of the crack tip domain illustrates that the degree of agreement is notably satisfactory with relative error lesser than a 5%, even for significantly large deformations.

Subsequently, the calculation of the configurational forces has been integrated with experimental tests on a soft elastomer. By explicitly replicating the experimental conditions within the numerical framework, i.e., constitutive behavior and geometrical features, we establish a direct link between both approaches. A crucial aspect of this process is the calibration of the material model. By solving a BVP that replicates the tensile deformation of the samples, and through the configurational force method as a post-processing algorithm, we have calculated the configurational forces at the crack tip. To that end, the BVP not only needs to reproduce the bulk tensile deformation, but also the more intricate crack tip deformation. To verify this requirement, we compare the numerical and experimental displacement fields, the former solved in the BVP, the latter obtained via DIC analysis. The absolute error field shows that the agreement at the crack tip adjoining area is reasonably accurate. Importantly, we believe that the slight discrepancies can be attributed to the limitations of the GNH model in reproducing the material behavior. The VHB tape typically displays a strain hardening exponent that is not perfectly constant. Nevertheless, this constitutive choice is necessary in order to exploit the finite strain analytical solution as done in Section 6. To the best of the authors' knowledge, analytical solutions for crack tip fields in soft materials are a rarity and the finite-strain analytical solution in Long and Hui (2015) provides an excellent means of validating the configurational force method at finite strains. By linking the configurational forces with the displacement field obtained from the virtual experiment, we demonstrate a reasonably satisfactory agreement. The configurational force method applied to the soft elastomer shows a satisfactory performance in the large deformation regime.

### 7.2. Outlook

The insights into the use of configurational forces presented in this study open new routes for future developments in modeling frameworks. After validating the configurational force method for approximating the $J$-integral in the context of a GNH material, the method consistently produces results which are as accurate as the quality in reproducing the geometric, load, and constitutive features. In this regard, future frameworks will accommodate any suitable constitutive model and will rely solely on configurational forces. As a consequence, the use of configurational forces in a standalone and reliable manner will eliminate the need for analytical close-form solutions, such as the traditional LEFM ones or the one explored in this manuscript for finite strains. Within this context, machine learning approaches hold promise to finely tune material behavior under various deformation modes and in the large deformation regime. Some timely works addressing this endeavor include Kirchdoerfer and Ortiz (2016), Fuhg and Bouklas (2022), Wiesheier et al. (2023), Gonzalez-Saiz and Garcia-Gonzalez (2023), Marino et al. (2023), Linka and Kuhl (2023) and Linden et al. (2023).

Building upon the previous outlook, future frameworks can be extended to delve into fracture onset conditions, strength evaluation, and configurational dissipation during crack propagation. These developments will enable the determination of the evolution of material positions in structures subjected to configurational forces acting on defects and boundaries. Such novel frameworks may also benchmark configurational forces at defects against a threshold parameter to implement fracture onset resistance, linked to constitutive attributes. Then, the evolution of the material positions may evolve according to an admissible configurational dissipation, e.g., akin to constitutive models for plastic deformation. To assist such configurational changes, computational frameworks based on peridynamics or shape optimization, among others, may be a promising starting point (Steinmann et al., 2023).

Since soft materials are customarily viscoelastic, the extension of the configurational force method for inelastic material behavior is particularly interesting. To achieve this, the deformation gradient is usually decomposed into elastic and inelastic parts. Then, the local balance of material momentum reveals a peculiarity. Unlike elastic material behavior, where the Eshelby stress is divergence-free, material inelasticity introduces a viscous material body force into the local balance statement (Nguyen et al., 2005; Kaliske et al., 2009). In the context of a crack propagating in a viscoelastic medium, only a portion of the far-field energy release rate supplied by the boundary conditions is delivered to the crack tip. The remainder is lost in the bulk material due to dissipation from inelastic processes. As a consequence, the global balance not only includes the crack-driving force (path-independent $J$-integral, the focus of fracture mechanics investigations) but also the path-dependent driving force related to inelastic dissipation, both compiled into a single quantity. To distinguish between these quantities, the viscous body forces can be calculated as the contraction of the spatial stress and the gradient of the inelastic strain, which evolves as an internal variable.

Further points of study may consider extensions to mixed-mode fracture problems and fully incompressible formulations. The extension of the framework to 3D mixed-mode fracture at finite strains will allow to apply the configurational force method to

interesting problems such as hydraulic fracture of shear-loaded hydrogels (Santarossa et al., 2023), osmotic instabilities (Wang et al., 2023), puncture failure mechanics (Liu et al., 2018), and cavitation in elastomers (Breedlove et al., 2023) and even in biological materials (Dougan et al., 2022), among others. To do so, additional challenges such as the calculation of line integrals along the crack faces need to be accounted for, as detailed in Schmitz and Ricoeur (2023). Likewise, the extension of the method with fully incompressible formulations, e.g., two- and three-field Lagrange multiplier method (Simo et al., 1985), will make the configurational force method physically consistent with soft polymers, which are nearly incompressible.

Moreover, and beyond the scope of soft fracture mechanics, the configurational force method can be applied to surface growth in soft material systems, encompassing a wide array of processes such as additive manufacturing technologies and diverse biological challenges. In the areas of tissue engineering, drug delivery, and soft robotics, the utilization of 3D- and 4D-printed soft polymers facilitates the design of intricate geometries and desired structural response (Chen et al., 2019; Xiang et al., 2020). In an additive manufacturing process, the flow of material, encompassing both mass creation and resorption, relates to the Eshelby energy–momentum tensor. Consequently, the thermodynamics framework must be extended as a second-order theory to account for the diffusion of mass (Epstein and Maugin, 2000). In hydrogels, such a framework may enable the modeling of substance diffusion within the material.

Likewise, we envisage the application of the configurational force method to architectured structures. Leveraging the knowledge of configurational forces on sharp interfaces (Abeyaratne and Knowles, 2000; Rajagopal and Sivakumar, 2007) and configurational-mechanics-based shape optimization (Riehl and Steinmann, 2014), composite laminates (Chen et al., 2023) and spinodoid topologies (Kumar et al., 2020b), inter alia, may use the configurational force method to optimize materials with targeted mechanical properties. In this regard, the method could be generalized in coupled problems for design purposes, e.g., electro-magneto-mechanics (Maugin et al., 1992) and flexoelectric solids (Tian et al., 2019; Moreno-Mateos, 2023).

## Code and data availability

The code and the data generated during the study is available via zenodo in https://doi.org/10.5281/zenodo.10577665.

## CRediT authorship contribution statement

**Miguel Angel Moreno-Mateos:** Conceptualization, Formal analysis, Investigation, Methodology, Software, Writing – original draft, Writing – review & editing. **Paul Steinmann:** Formal analysis, Funding acquisition, Writing – review & editing.

## Declaration of competing interest

The authors declare the following financial interests/personal relationships which may be considered as potential competing interests: Miguel Angel Moreno-Mateos reports financial support was provided by European Research Council. Paul Steinmann reports financial support was provided by European Research Council.

## Acknowledgments

The authors acknowledge support from the European Research Council (ERC) under the Horizon Europe program (Grant-No. 101052785, project: SoftFrac).

## Appendix A. Calibration of the Generalized neo-Hookean model

The calibration of the GNH model is done from tensile tests on bulk uncut samples with initial length of $30\,\mathrm{mm}$ and a same quasi-static loading rate of $0.02\,\mathrm{mm\,s^{-1}}$, i.e., strain rate of $6.7\times10^{-4}\,\mathrm{s^{-1}}$. A virtual tensile test mimicking the experimental sample and setup is used to fit the output stress–displacement curve to the experimental one by adjusting the input constitutive parameters: the shear modulus $G$, the exponent $n$, and the coefficient $b$. Their values are shown in Fig. A.13.

Given that the analytical solution in Eq. (13) is built upon the GNH model, the FE framework for the calculation of the configurational forces needs to implement the same constitutive model. Therefore, the use of the GNH is necessary to enable the comparison of the material forces and the values of $J$ estimated experimentally. On the whole, the model adequately captures the constitutive response under tensile loading. Nevertheless, alternative models specifically designed to reproduce the initial strain softening, following plateau, and eventually strain hardening of elastomers may be a convenient alternative choice to model the response of VHB tape.

## Appendix B. Configurational forces on Pacman-shaped domains without spurious forces

An alternative approach to compute the total configurational force is the crack tip evaluation. This approach entails not adding up the spurious forces around the crack tip in the calculation of the total configurational force. Fig. B.14 presents the outcomes, which render a less accurate approximation of the $J$-integral.

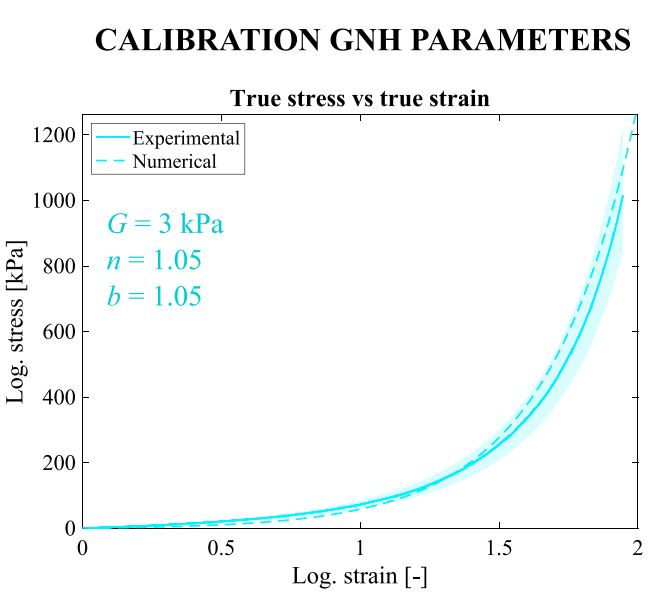


**Fig. A.13. Calibration of the GNH model from tensile tests on uncut samples.** The numerical model reproducing a sample without initial pre-cut produces a stress–strain curve that is fitted to the experimental one via adjustment of the constitutive parameters of the GNH model. The experimental mean curve from three experimental repetitions is calculated and a scatter area is included to quantify the experimental variability.

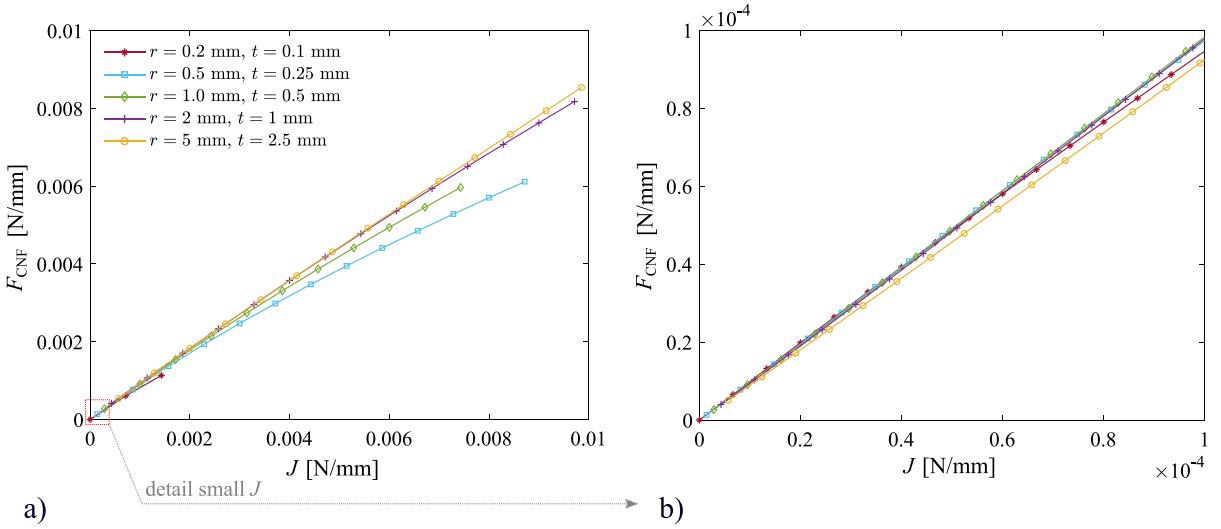


**Fig. B.14. Evolution of the total configurational force at the crack front of the Pacman-shaped domains subjected to $J$-controlled loading.** (a) The evolution of $F_{\text{CNF}}$ is plotted against $J$ for all the radii and thicknesses utilized to define the Pacman domains: $r = \{0.2, 0.5, 1, 2, 5\}$ mm and $t = \{0.1, 0.25, 0.5, 1, 2.5\}$ mm, respectively for each domain. (b) Detail for small values of $J$. The total force $F_{\text{CNF}}$ is obtained adding up all the nodal forces at the crack edge. The constitutive model is neo-Hookean ($n = 1$, $b = 1$).

## Appendix C. Experimental validation of $J$-integral via finite strain analytical solution

Section 6 provided a comparison between configurational forces and the $J$-integral estimated from numerical fields using the analytical solution. Here, a similar approach is taken, but $J$ is estimated from the experimental fields instead. This comparison, although less ideal, provides insightful results and is illustrated in Fig. C.15.

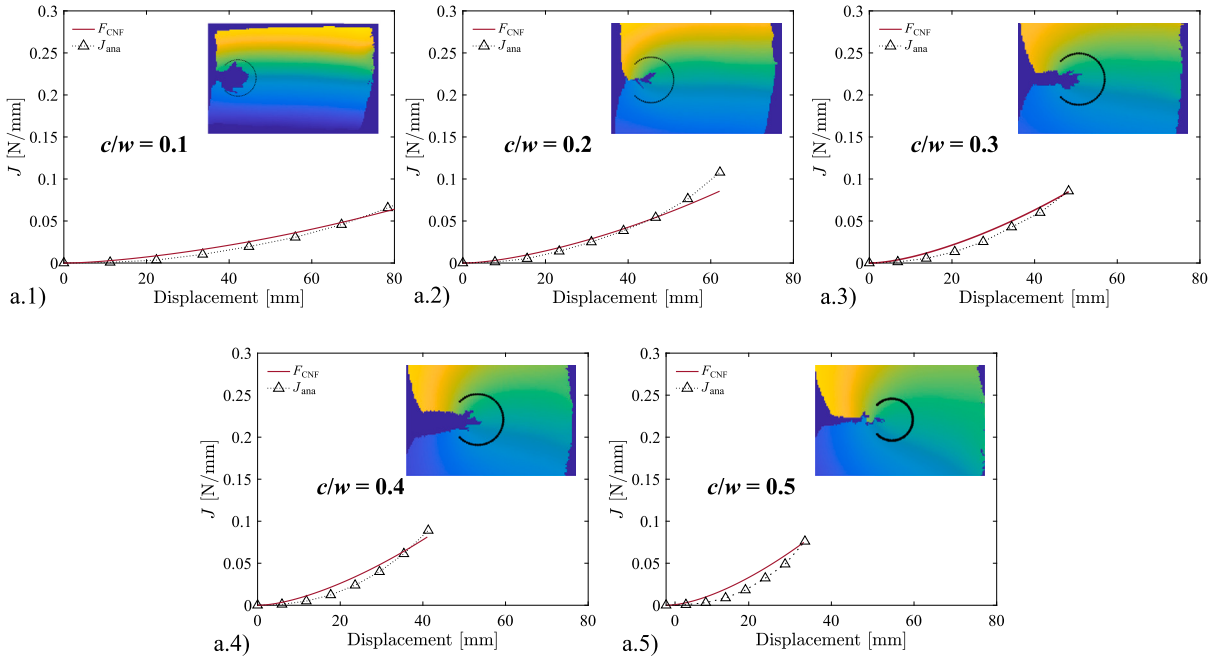


**Fig. C.15. Results for $J$-integral estimated from experimental displacement fields and comparison with configurational forces.** The displacement fields used to fit $J$ are extracted from the DIC results. An annular grid sufficiently close to the crack tip is used for the fitting and depicted with black points. The performance of the configurational force ($F_{CNF}$) to replicate the $J$-integral is validated for the different crack-width ratios $c/w$: (a) 0.1, (b) 0.2, (c) 0.3, (d) 0.4, and (e) 0.5, and for a discrete number of displacements (triangle markers).

## References


Abeyaratne, R., Knowles, J.K., 2000. A note on the driving traction acting on a propagating interface: Adiabatic and non-adiabatic processes of a continuum. J. Appl. Mech. 67, 829–830.

Ahmad, D., Sahu, S.K., Patra, K., 2019. Fracture toughness, hysteresis and stretchability of dielectric elastomers under equibiaxial and biaxial loading. Polym. Test. 79, 106038.

Armanini, C., Corso, F.D., Misseroni, D., Bigoni, D., 2019. Configurational forces and nonlinear structural dynamics. J. Mech. Phys. Solids 130, 82–100.

Bai, R., Yang, J., Suo, Z., 2019. Fatigue of hydrogels. Eur. J. Mech. A Solids 74, 337–370.

Baktheer, A., Martínez-Pañeda, E., Aldakheel, F., 2024. Phase field cohesive zone modeling for fatigue crack propagation in quasi-brittle materials. Comput. Methods Appl. Mech. Engrg. 422, 116834.

Barati, E., Alizadeh, Y., Aghazadeh, J., Berto, F., 2010. Some new practical equations for rapid calculation of j-integral in plates weakened by u-notches under bending. Mater. Des. 31, 2964–2971.

Baxevanakis, K.P., Giannakopoulos, A.E., 2015. Finite element analysis of discrete edge dislocations: Configurational forces and conserved integrals. Int. J. Solids Struct. 62, 52–65.

Belytschko, T., Lu, Y.Y., Gu, L., Tabbara, M., 1995. Element-free Galerkin methods for static and dynamic fracture. Int. J. Solids Struct. 32, 2547–2570.

Blaber, J., Adair, B., Antoniou, A., 2015. NCorr: Open-source 2d digital image correlation matlab software. Exp. Mech. 55, 1105–1122.

Braun, M., 1997. Configurational forces induced by finite-element discretization. Proc. Est. Acad. Sci. Phys. Math. 46, 24–31.

Braun, M., Iváñez, I., Ariza, M., 2024. A discrete lattice model with axial and angular springs for modeling fracture in fiber-reinforced composite laminates. Eur. J. Mech. A Solids 104, 105213.

Breedlove, E., Chen, C., Lindeman, D., Lopez-Pamies, O., 2023. Cavitation in elastomers: A review of the evidence against elasticity. 12.

Brezzi, F., Fortin, M., 1991. Mixed and Hybrid Finite Element Methods, vol. 15, Springer New York.

Chen, V.W., Arora, N., Goshkoderia, A., Willey, C.L., Turgut, Z., Buskohl, P.R., Rudykh, S., Juhl, A.T., 2023. Mechanical instability tuning of a magnetorheological elastomer composite laminate. Composites B 251, 110472.

Chen, C., Wang, Z., Suo, Z., 2017. Flaw sensitivity of highly stretchable materials. Extreme Mech. Lett. 10, 50–57.

Chen, L., Yang, S., 2022. Electro-cavitation and electro-assisted snap-through instability of a hollow sphere of dielectric elastomers. Thin-Walled Struct. 181, 109995.

Chen, Z., Zhao, D., Liu, B., Nian, G., Li, X., Yin, J., Qu, S., Yang, W., 2019. 3D printing of multifunctional hydrogels. Adv. Funct. Mater. 29, 1900971.

Cherepanov, G.P., 1967. Crack propagation in continuous media. J. Appl. Math. Mech. 31, 503–512.

Chihadeh, A., Storm, J., Kaliske, M., 2023. Fracture modeling by the eigenfracture approach for the implicit material point method framework. Internat. J. Numer. Methods Engrg. 124, 1280–1306.

Creton, C., Ciccotti, M., 2016. Fracture and adhesion of soft materials: a review. Rep. Progr. Phys. 79, 046601.

Denzer, R., Barth, F.J., Steinmann, P., 2003. Studies in elastic fracture mechanics based on the material force method. Internat. J. Numer. Methods Engrg. 58, 1817–1835.

Denzer, R., Menzel, A., 2014. Configurational forces for quasi-incompressible large strain electro-viscoelasticity – application to fracture mechanics. Eur. J. Mech. A Solids 48, 3–15.

Diehl, P., Lipton, R., Wick, T., Tyagi, M., 2022. A comparative review of peridynamics and phase-field models for engineering fracture mechanics. Comput. Mech. 69, 1259–1293.

Dougan, C.E., Song, Z., Fu, H., Crosby, A.J., Cai, S., Peyton, S.R., 2022. Cavitation induced fracture of intact brain tissue. Biophys. J. 121, 2721–2729.
Dugdale, D., 1960. Yielding of steel sheets containing slits. J. Mech. Phys. Solids 8, 100–104.
Epstein, M., Maugin, G.A., 2000. Thermomechanics of volumetric growth in uniform bodies. Int. J. Plast. 16, 951–978.
Erdogan, F., Sih, G.C., 1963. On the crack extension in plates under plane loading and transverse shear. J. Basic Eng. 85, 519–525.
Eshelby, J.D., 1951. The force on an elastic singularity. Philos. Trans. R. Soc. Lond. 244.
Eshelby, J.D., 1975. The elastic energy–momentum tensor. J. Elasticity 5, 321–335.
Eshelby, J.D., 1999. Energy relations and the energy–momentum tensor in continuum mechanics. In: Fundamental Contributions to the Continuum Theory of Evolving Phase Interfaces in Solids. pp. 82–119.
Fan, Z., Liao, H., Jiang, H., Wang, H., Li, B., 2021. A dynamic adaptive eigenfracture method for failure in brittle materials. Eng. Fract. Mech. 244, 107540.
Fischer, F.D., Simha, N.K., Predan, J., Schöngrundner, R., Kolednik, O., 2012. On configurational forces at boundaries in fracture mechanics. Int. J. Fract. 174, 61–74.
Francfort, G.A., Marigo, J.J., 1998. Revisiting brittle fracture as an energy minimization problem. J. Mech. Phys. Solids 46, 1319–1342.
Frankl, S.M., Pletz, M., Schuecker, C., 2022. Improved concept for iterative crack propagation using configurational forces for targeted angle correction. Eng. Fract. Mech. 266, 108403.
Fu, Y., Lu, H., Nian, G., Wang, P., Lin, N., Hu, X., Zhou, H., Yu, H., Qu, S., Yang, W., 2020. Size-dependent inertial cavitation of soft materials. J. Mech. Phys. Solids 137, 103859.
Fuhg, J.N., Bouklas, N., 2022. On physics-informed data-driven isotropic and anisotropic constitutive models through probabilistic machine learning and space-filling sampling. Comput. Methods Appl. Mech. Engrg. 394, 114915.
Gao, Y., Han, X., Chen, J., Pan, Y., Yang, M., Lu, L., Yang, J., Suo, Z., Lu, T., 2021. Hydrogel–mesh composite for wound closure. Proc. Natl. Acad. Sci. 118.
Geubelle, P.H., Knauss, W.G., 1994. Finite strains at the tip of a crack in a sheet of hyperelastic material: I. homogeneous case. J. Elasticity 35, 61–98.
Goda, I., Ganghoffer, J.F., Maurice, G., 2016. Combined bone internal and external remodeling based on eshelby stress. Int. J. Solids Struct. 94–95, 138–157.
Gonzalez-Saiz, E., Garcia-Gonzalez, D., 2023. Model-driven identification framework for optimal constitutive modeling from kinematics and rheological arrangement. Comput. Methods Appl. Mech. Engrg. 415, 116211.
Griffith, A.A., 1921. The phenomena of rupture and flow in solids. Phil. Trans. R. Soc. A 221, 163–198.
Gross, D., Kolling, S., Mueller, R., Schmidt, I., 2003. Configurational forces and their application in solid mechanics. Eur. J. Mech. A Solids 22, 669–692.
Guo, Y., Li, Q., 2017. Material configurational forces applied to mixed mode crack propagation. Theor. Appl. Fract. Mech. 89, 147–157.
Gurtin, M.E., Podio-Guidugli, P., 1996. Configurational forces and the basic laws for crack propagation. J. Mech. Phys. Solids 44, 905–927.
Hedan, S., Valle, V., Cottron, M., 2011. Calculation of j-integrals using experimental and numerical data: Influences of ratio (A/W) and the 3d structure. Eng. Fract. Mech. 78, 1976–1985.
Heider, Y., 2021. A review on phase-field modeling of hydraulic fracturing. Eng. Fract. Mech. 253, 107881.
Hénap, G., Szabó, L., 2017. On the configurational-force-based r-adaptive mesh refinement in isogeometric analysis. Finite Elem. Anal. Des. 124, 1–6.
Hesch, C., Gil, A.J., Ortigosa, R., Dittmann, M., Bilgen, C., Betsch, P., Franke, M., Janz, A., Weinberg, K., 2017. A framework for polyconvex large strain phase-field methods to fracture. Comput. Methods Appl. Mech. Engrg. 317, 649–683.
Hocine, N.A., Abdelaziz, M.N., Imad, A., 2002. Fracture problems of rubbers: J-integral estimation based upon $\mu$ factors and an investigation on the strain energy density distribution as a local criterion. Int. J. Fract. 117, 1–23.
Hossain, M., Vu, D.K., Steinmann, P., 2012. Experimental study and numerical modelling of VHB 4910 polymer. Comput. Mater. Sci. 59, 65–74.
Hui, C.Y., Jagota, A., Bennison, S.J., Londono, J.D., 2003. Crack blunting and the strength of soft elastic solids. Proc. R. Soc. Lond. Ser. A Math. Phys. Eng. Sci. 459, 1489–1516.
Hussain, M., Pu, S., Underwood, J., 1974. Strain energy release rate for a crack under combined mode i and mode ii. In: National Symposium on Fracture Mechanics, Vol. 3. 2–2–27.
Irwin, G., 1957. Analysis of stresses and strains near the end of a crack traversing a plate. J. Appl. Mech. 24, 361–364.
Javili, A., Ekiz, E., McBride, A.T., Steinmann, P., 2021. Continuum-kinematics-inspired peridynamics: Thermo-mechanical problems. Contin. Mech. Thermodyn. 33, 2039–2063.
Jirásek, M., 1998. Nonlocal models for damage and fracture: Comparison of approaches. Int. J. Solids Struct. 35, 4133–4145.
Kalina, M., Schneider, T., Brummund, J., Kästner, M., 2023. Overview of phase-field models for fatigue fracture in a unified framework. Eng. Fract. Mech. 288, 109318.
Kaliske, M., Netzker, C., Näser, B., 2009. Evaluation of crack-driving forces at finite viscoelasticity: Theory and experiment. IUTAM Bookser. 17, 193–202.
Kienzler, R., Herrmann, G., 1997. On the properties of the eshelby tensor. Acta Mech. 125, 73–91.
Kienzler, R., Herrmann, G., Haslach, H., 2002. Mechanics in material space: With applications to defect and fracture mechanics. Appl. Mech. Rev. 55, B23–B24.
Kirchdoerfer, T., Ortiz, M., 2016. Data-driven computational mechanics. Comput. Methods Appl. Mech. Engrg. 304, 81–101.
Kirchner, H.O., Lazar, M., 2007. The thermodynamic driving force for bone growth and remodelling: a hypothesis. J. R. Soc. Interface 5, 183–193.
Kolednik, O., Predan, J., Fischer, F.D., 2010. Cracks in inhomogeneous materials: Comprehensive assessment using the configurational forces concept. Eng. Fract. Mech. 77, 2698–2711.
Kolednik, O., Tiwari, A., Posch, C., Kegl, M., 2022. Configurational force based analysis of creep crack growth. Int. J. Fract. 236, 175–199.
Kuhl, E., Denzer, R., Barth, F.J., Steinmann, P., 2004. Application of the material force method to thermo-hyperelasticity. Comput. Methods Appl. Mech. Engrg. 193, 3303–3325.
Kuhl, E., Steinmann, P., 2004. Computational modeling of healing: An application of the material force method. Biomech. Model. Mechanobiol. 2, 187–203.
Kumar, A., Bourdin, B., Francfort, G.A., Lopez-Pamies, O., 2020a. Revisiting nucleation in the phase-field approach to brittle fracture. J. Mech. Phys. Solids 142, 104027.
Kumar, S., Tan, S., Zheng, L., Kochmann, D.M., 2020b. Inverse-designed spinodoid metamaterials. npj Comput. Mater. 6, 73.
Larsen, C.J., Dolbow, J.E., Lopez-Pamies, O., 2024. A variational formulation of griffith phase-field fracture with material strength. 1.
Lefèvre, V., Ravi-Chandar, K., Lopez-Pamies, O., 2015. Cavitation in rubber: an elastic instability or a fracture phenomenon? Int. J. Fract. 192, 1–23.
Li, M., Chen, L., Li, Y., Dai, X., Jin, Z., Zhang, Y., Feng, W., Yan, L.T., Cao, Y., Wang, C., 2022. Superstretchable, yet stiff, fatigue-resistant ligament-like elastomers. Nature Commun. 13, 1–8.
Li, P., Li, W., Li, B., Yang, S., Shen, Y., Wang, Q., Zhou, K., 2023. A review on phase field models for fracture and fatigue. Eng. Fract. Mech. 289, 109419.
Li, C., Yang, H., Suo, Z., Tang, J., 2020. Fatigue-resistant elastomers. J. Mech. Phys. Solids 134, 103751.
Liao, Z., Hossain, M., Yao, X., Mehnert, M., Steinmann, P., 2020. On thermo-viscoelastic experimental characterization and numerical modelling of VHB polymer. Int. J. Non-Linear Mech. 118, 103263.
Linden, L., Klein, D.K., Kalina, K.A., Brummund, J., Weeger, O., Kästner, M., 2023. Neural networks meet hyperelasticity: A guide to enforcing physics. J. Mech. Phys. Solids 179, 105363.
Linka, K., Kuhl, E., 2023. A new family of constitutive artificial neural networks towards automated model discovery. Comput. Methods Appl. Mech. Engrg. 403, 115731.
Liu, J., Chen, Z., Liang, X., Huang, X., Mao, G., Hong, W., Yu, H., Qu, S., 2018. Puncture mechanics of soft elastomeric membrane with large deformation by rigid cylindrical indenter. J. Mech. Phys. Solids 112, 458–471.

Liu, R., Hou, J., Li, Q., 2020. Material configurational forces applied to mixed-mode fatigue crack propagation and life prediction in elastic–plastic material. Int. J. Fatigue 134, 105467.
Lo, Y.-S., Hughes, T.J., Landis, C.M., 2022. Phase-field fracture modeling for large structures. J. Mech. Phys. Solids 105118.
Logg, A., Mardal, K.-A., Wells, G., eds, 2012. Automated Solution of Differential Equations by the Finite Element Method, vol. 84, Springer Berlin Heidelberg.
Long, R., Hui, C.-Y., 2015. Crack tip fields in soft elastic solids subjected to large quasi-static deformation — a review. Extreme Mech. Lett. 4, 131–155.
Long, R., Hui, C.-Y., 2016. Fracture toughness of hydrogels: measurement and interpretation. Soft Matter 12, 8069–8086.
Long, R., Krishnan, V.R., Hui, C.Y., 2011. Finite strain analysis of crack tip fields in incompressible hyperelastic solids loaded in plane stress. J. Mech. Phys. Solids 59, 672–695.
Lu, Y., Qi, Y., Tenardi, M., Long, R., 2021. Mixed-mode fracture in a soft elastomer. Extreme Mech. Lett. 48, 101380.
Ma, Z., Bourquard, C., Gao, Q., Jiang, S., Iure-Grimmel, T.D., Huo, R., Li, X., He, Z., Yang, Z., Yang, G., Wang, Y., Lam, E., hua Gao, Z., Supponen, O., Li, J., 2022. Controlled tough bioadhesion mediated by ultrasound. Science 377, 751–755.
Ma, L., Lu, T.J., Korsunsky, A.M., 2006. Vector j-integral analysis of crack interaction with pre-existing singularities. J. Appl. Mech. 73, 876–883.
Marigo, J.J., 2023. Modelling of fracture by cohesive force models: A path to pursue. Eur. J. Mech. A Solids 102, 105088.
Marino, E., Flaschel, M., Kumar, S., Lorenzis, L.D., 2023. Automated identification of linear viscoelastic constitutive laws with euclid. Mech. Mater. 181, 104643.
Maugin, G.A., Epstein, M., Trimarco, C., 1992. Pseudomomentum and material forces in inhomogeneous materials: Application to the fracture of electromagnetic materials in electromagnetoelastic fields. Int. J. Solids Struct. 29, 1889–1900.
Menzel, A., Denzer, R., Steinmann, P., 2004. On the comparison of two approaches to compute material forces for inelastic materials. Application to single-slip crystal-plasticity. Comput. Methods Appl. Mech. Engrg. 193, 5411–5428.
Menzel, A., Denzer, R., Steinmann, P., 2005. Material forces in computational single-slip crystal-plasticity. Comput. Mater. Sci. 32, 446–454.
Miehe, C., Hofacker, M., Welschinger, F., 2010a. A phase field model for rate-independent crack propagation: Robust algorithmic implementation based on operator splits. Comput. Methods Appl. Mech. Engrg. 199, 2765–2778.
Miehe, C., Welschinger, F., Hofacker, M., 2010b. Thermodynamically consistent phase-field models of fracture: Variational principles and multi-field Fe implementations. Internat. J. Numer. Methods Engrg. 83, 1273–1311.
Moës, N., Dolbow, J., Belytschko, T., 1999. A finite element method for crack growth without remeshing. Internat. J. Numer. Methods Engrg..
Moreno-Mateos, M.A., 2023. A gradient micromechanical model to explore flexoelectric copolymers via stochastic chain growth. Eur. J. Mech. A Solids 102, 105106.
Moreno-Mateos, M.A., Danas, K., Garcia-Gonzalez, D., 2023a. Influence of magnetic boundary conditions on the quantitative modelling of magnetorheological elastomers. Mech. Mater. 184, 104742.
Moreno-Mateos, M.A., Hossain, M., Steinmann, P., Garcia-Gonzalez, D., 2022. Hybrid magnetorheological elastomers enable versatile soft actuators. npj Comput. Mater. 8, 162.
Moreno-Mateos, M.A., Hossain, M., Steinmann, P., Garcia-Gonzalez, D., 2023b. Hard magnetics in ultra-soft magnetorheological elastomers enhance fracture toughness and delay crack propagation. J. Mech. Phys. Solids 173, 105232.
Moreno-Mateos, M.A., Mehnert, M., Steinmann, P., 2024. Electro-mechanical actuation modulates fracture performance of soft dielectric elastomers. Internat. J. Engrg. Sci. 195, 104008.
Näser, B., Kaliske, M., Müller, R., 2007. Material forces for inelastic models at large strains: Application to fracture mechanics. Comput. Mech. 40, 1005–1013.
Nguyen, T.D., Govindjee, S., Klein, P.A., Gao, H., 2005. A material force method for inelastic fracture mechanics. J. Mech. Phys. Solids 53, 91–121.
Özenç, K., Chinaryan, G., Kaliske, M., 2016. A configurational force approach to model the branching phenomenon in dynamic brittle fracture. Eng. Fract. Mech. 157, 26–42.
Özenç, K., Kaliske, M., Lin, G., Bhashyam, G., 2014. Evaluation of energy contributions in elasto-plastic fracture: A review of the configurational force approach. Eng. Fract. Mech. 115, 137–153.
Park, K., Paulino, G.H., 2011. Cohesive zone models: A critical review of traction-separation relationships across fracture surfaces. Appl. Mech. Rev. 64.
Peach, M., Koehler, J.S., 1950. The forces exerted on dislocations and the stress fields produced by them. Phys. Rev. 80, 436.
Peerlings, R., de Borst, R., Brekelmans, W., Geers, M., 1998. Gradient-enhanced damage modelling of concrete fracture. Mech. Cohesive-Frictional Mater. 3, 323–342.
Pharr, M., Sun, J.Y., Suo, Z., 2012. Rupture of a highly stretchable acrylic dielectric elastomer. J. Appl. Phys. 111.
Podio-Guidugli, P., 2002. Configurational forces: are they needed? Mech. Res. Commun. 29, 513–519.
Qi, Y., Zou, Z., Xiao, J., Long, R., 2019. Mapping the nonlinear crack tip deformation field in soft elastomer with a particle tracking method. J. Mech. Phys. Solids 125, 326–346.
Rajagopal, A., Sivakumar, S.M., 2007. A combined r-h adaptive strategy based on material forces and error assessment for plane problems and bimaterial interfaces. Comput. Mech. 41, 49–72.
Rice, J.R., 1968. A path independent integral and the approximate analysis of strain concentration by notches and cracks. J. Appl. Mech. 35, 379.
Ricker, S., Mergheim, J., Steinmann, P., Müller, R., 2010. A comparison of different approaches in the multi-scale computation of configurational forces. Int. J. Fract. 166, 203–214.
Riehl, S., Steinmann, P., 2014. An integrated approach to shape optimization and mesh adaptivity based on material residual forces. Comput. Methods Appl. Mech. Engrg. 278, 640–663.
Rohracker, M., Kumar, P., Mergheim, J., 2023. A comparative assessment of different adaptive spatial refinement strategies in phase-field fracture models for brittle fracture. Forces Mech. 10, 100157.
Russ, J., Slesarenko, V., Rudykh, S., Waisman, H., 2020. Rupture of 3d-printed hyperelastic composites: Experiments and phase field fracture modeling. J. Mech. Phys. Solids 140, 103941.
Sanoja, G.E., Morelle, X.P., Comtet, J., Yeh, C.J., Ciccotti, M., Creton, C., 2021. Why is mechanical fatigue different from toughness in elastomers? the role of damage by polymer chain scission. Sci. Adv. 7.
Santarossa, A., Ortellado, L., Sack, A., Gómez, L.R., Pöschel, T., 2023. A device for studying fluid-induced cracks under mixed-mode loading conditions using X-ray tomography. Rev. Sci. Instrum. 94.
Schmidt, B., Fraternali, F., Ortiz, M., 2009. Eigenfracture: An eigendeformation approach to variational fracture. 7, pp. 1237–1266. http://dx.doi.org/10.1137/080712568.
Schmitz, K., Ricoeur, A., 2023. Theoretical and computational aspects of configurational forces in three-dimensional crack problems. Int. J. Solids Struct. 282, 112456.
Schreyer, H.L., 1990. Analytical solutions for nonlinear strain-gradient softening and localization. J. Appl. Mech. 57, 522–528.
Schütte, H., 2009. Curved crack propagation based on configurational forces. Comput. Mater. Sci. 46, 642–646.
Shih, C.F., Moran, B., Nakamura, T., 1986. Energy release rate along a three-dimensional crack front in a thermally stressed body. Int. J. Fract. 30, 79–102.
Sih, G.C., 1974. Strain–energy-density factor applied to mixed mode crack problems. Int. J. Fract. 10, 305–321.
Silling, S.A., 2000. Reformulation of elasticity theory for discontinuities and long-range forces. J. Mech. Phys. Solids 48, 175–209.
Simha, N.K., Fischer, F.D., Shan, G.X., Chen, C.R., Kolednik, O., 2008. J-integral and crack driving force in elastic–plastic materials. J. Mech. Phys. Solids 56, 2876–2895.

Simo, J.C., Taylor, R.L., Pister, K.S., 1985. Variational and projection methods for the volume constraint in finite deformation elasto-plasticity. Comput. Methods Appl. Mech. Engrg. 51, 177–208.
Song, J.H., Wang, H., Belytschko, T., 2008. A comparative study on finite element methods for dynamic fracture. Comput. Mech. 42, 239–250.
Spagnoli, A., Brighenti, R., Montanari, M., Terzano, M., 2023. Crack-tip blunting and its implications on fracture of soft materials. Fatigue Fract. Eng. Mater. Struct. 46, 1627–1637.
Steinmann, P., 2000. Application of material forces to hyperelastostatic fracture mechanics. I. continuum mechanical setting. Int. J. Solids Struct. 37, 7371–7391.
Steinmann, P., 2002. On spatial and material settings of hyperelastostatic crystal defects. J. Mech. Phys. Solids 50, 1743–1766.
Steinmann, P., 2008. On boundary potential energies in deformational and configurational mechanics. J. Mech. Phys. Solids 56, 772–800.
Steinmann, P., 2022. Spatial and Material Forces in Nonlinear Continuum Mechanics, vol. 272, Springer International Publishing.
Steinmann, P., Ackermann, D., Barth, F., 2001. Application of material forces to hyperelastostatic fracture mechanics. II. computational setting. Int. J. Solids Struct. 38, 5509–5526.
Steinmann, P., de Villiers, A., McBride, A., Javili, A., 2023. Configurational peridynamics. Mech. Mater. 185, 104751.
Steinmann, P., Scherer, M., Denzer, R., 2009. Secret and joy of configurational mechanics: From foundations in continuum mechanics to applications in computational mechanics. ZAMM Z. Angew. Math. Mech. (J. Appl. Math. Mech.) 89, 614–630.
Storm, J., Kaliske, M., 2023a. The origin of the energy split in phase-field fracture and eigenfracture. PAMM 23, e202300295.
Storm, J., Kaliske, M., 2023b. Phase-field fracture based on representative crack elements (RCE): Inelastic materials, friction, finite deformations, multi-physics. PAMM 22, e202100156.
Strifors, H.C., 1974. A generalized force measure of conditions at crack tips. Int. J. Solids Struct. 10, 1389–1404.
Tang, J., Li, J., Vlassak, J.J., Suo, Z., 2017. Fatigue fracture of hydrogels. Extreme Mech. Lett. 10, 24–31.
Taylor, D., O'Mara, N., Ryan, E., Takaza, M., Simms, C., 2012. The fracture toughness of soft tissues. J. Mech. Behav. Biomed. Mater. 6, 139–147.
Theocharidis, G., Yuk, H., Roh, H., Wang, L., Mezghani, I., Wu, J., Kafanas, A., Contreras, M., Sumpio, B., Li, Z., Wang, E., Chen, L., Guo, C.F., Jayaswal, N., Katopodi, X.-L., Kalavros, N., Nabzdyk, C.S., Vlachos, I.S., Veves, A., Zhao, X., 2022. A strain-programmed patch for the healing of diabetic wounds. Nat. Biomed. Eng. 1–16.
Tian, X., Li, Q., Deng, Q., 2019. The j-integral in flexoelectric solids. Int. J. Fract. 215, 67–76.
Vavrik, D., Jandejsek, I., 2014. Experimental evaluation of contour j integral and energy dissipated in the fracture process zone. Eng. Fract. Mech. 129, 14–25.
Wang, C., Chen, X., Wang, L., Makihata, M., Liu, H.-C., Zhou, T., Zhao, X., 2022. Bioadhesive ultrasound for long-term continuous imaging of diverse organs. Science 377, 517–523.
Wang, Z., Liu, J., Chen, P., Suo, Z., 2023. Osmotic instability in soft materials under well-controlled triaxial stress. J. Mech. Phys. Solids 172, 105195.
Wells, A., 1961. Unstable crack propagation in metals: Cleavage and fast fracture. In: Proceedings of the Crack Propagation Symposium, Vol. 1. paper 84. Crack Tip Opening Displacement (CTOD).
Wiesheier, S., Mergheim, J., Steinmann, P., 2023. Discrete data-adaptive approximation of hyperelastic energy functions. Comput. Methods Appl. Mech. Engrg. 416, 116366.
Xiang, Y., Schilling, C., Arora, N., Boydston, A.J., Rudykh, S., 2020. Mechanical characterization and constitutive modeling of visco-hyperelasticity of photocured polymers. Addit. Manuf. 36, 101511.
Xue, N., Long, R., Dufresne, E.R., Style, R.W., 2023. Strain-stiffening elastomers fail from the edge. p. 6.
Yan, S., Schlüter, A., Müller, R., 2023. Configurational forces in a phase field model for fatigue. PAMM 22, e202200034.
Yin, T., Wu, T., Liu, J., Qu, S., Yang, W., 2021. Essential work of fracture of soft elastomers. J. Mech. Phys. Solids 156, 104616.
Yuk, H., Zhang, T., Parada, G.A., Liu, X., Zhao, X., 2016. Skin-inspired hydrogel–elastomer hybrids with robust interfaces and functional microstructures. Nature Commun. 7, 1–11.
Zheng, D., Lin, S., Ni, J., Zhao, X., 2022. Fracture and fatigue of entangled and unentangled polymer networks. Extreme Mech. Lett. 51, 101608.
Zhou, R., Coombs, W.M., Xu, Y., Zhang, P., Wang, L.G., 2022. A configurational force-based material point method for crack propagation modelling in 2d. Theor. Appl. Fract. Mech. 117, 103186.